

1 Structure, mutagenesis and QM:MM modelling of
2 3-ketosteroid Δ^1 -dehydrogenase from
3 *Sterolibacterium denitrificans* – the role of new
4 putative membrane-associated domain and proton-
5 relay system in catalysis

6 *Patrycja Wójcik¹, Michał Glanowski¹, Beata Mrugała¹, Magdalena Prochner^{1,2}, Olga*
7 *Zastawny¹, Monika Flejszar^{1,3}, Katarzyna Kurpiewska⁴, Ewa Niedziałkowska⁵, Wlodek*
8 *Minor⁶, Maria Oszajca⁴, Andrzej J. Bojarski², Agnieszka M. Wojtkiewicz¹, Maciej Szaleniec^{1,*}*

9 ¹Jerzy Haber Institute of Catalysis and Surface Chemistry, Polish Academy of Sciences,
10 Niezapominajek 8, 30-239 Krakow, Poland

11 ²Jerzy Maj Institute of Pharmacology Polish Academy of Sciences, Smętna 12, 31-343
12 Krakow, Poland

13 ³Department of Physical Chemistry, Faculty of Chemistry, Rzeszow University of
14 Technology, Al. Powstańców Warszawy 6, 35-959 Rzeszów, Poland

15 ⁴ Faculty of Chemistry, Jagiellonian University, Gronostajowa 2, 30-387 Kraków, Poland

16 ⁵Department of Molecular Physiology and Biological Physics, University of Virginia, 200
17 Jeanette Lancaster Way Charlottesville, VA, USA

18 ⁶ Department of Molecular Physiology and Biological Physics, University of Virginia, 1340
19 Jefferson Park Av. Jordan Hall Charlottesville, VA, USA

20 *email: maciej.szaleniec@ikifp.edu.pl

21 KEYWORDS: ketosteroid Δ^1 -dehydrogenase, 3-ketosteroids, Δ^1 -dehydrogenation, kinetic
22 isotope effect, 3-ketosteroid dehydrogenase

23 ABSTRACT:

24 3-Ketosteroid Δ^1 -dehydrogenases (KstD) are important microbial flavin enzymes that initiate
25 the metabolism of steroid ring A and find application in the synthesis of steroid drugs. We
26 present a structure of the KstD from *Sterolibacterium denitrificans* (AcmB), which contains a
27 previously uncharacterized putative membrane-associated domain and extended proton-relay
28 system. The experimental and theoretical studies show that the steroid Δ^1 -dehydrogenation
29 proceeds according to the Ping-Pong bi-bi kinetics and a two-step base-assisted elimination
30 (E2cB) mechanism. The mechanism is validated by evaluating the experimental and theoretical
31 kinetic isotope effect for deuterium substituted substrates. The role of the active site residues is
32 quantitatively assessed by point mutations, experimental activity assays, and QM/MM MD
33 modelling of the reductive half-reaction (RHR). The pre-steady-state kinetics also reveals that
34 the low pH (6.5) optimum of AcmB is dictated by the oxidative half-reaction (OHR), while the
35 RHR exhibits a slight optimum at the pH usual for the KstD family of 8.5. The modelling
36 confirms the origin of the enantioselectivity of C2-H activation and substrate specificity for Δ^4 -
37 3-ketosteroids. Finally, the cholest-4-en-3-one turns out to be the best substrate of AcmB in
38 terms of ΔG of binding and predicted rate of dehydrogenation.

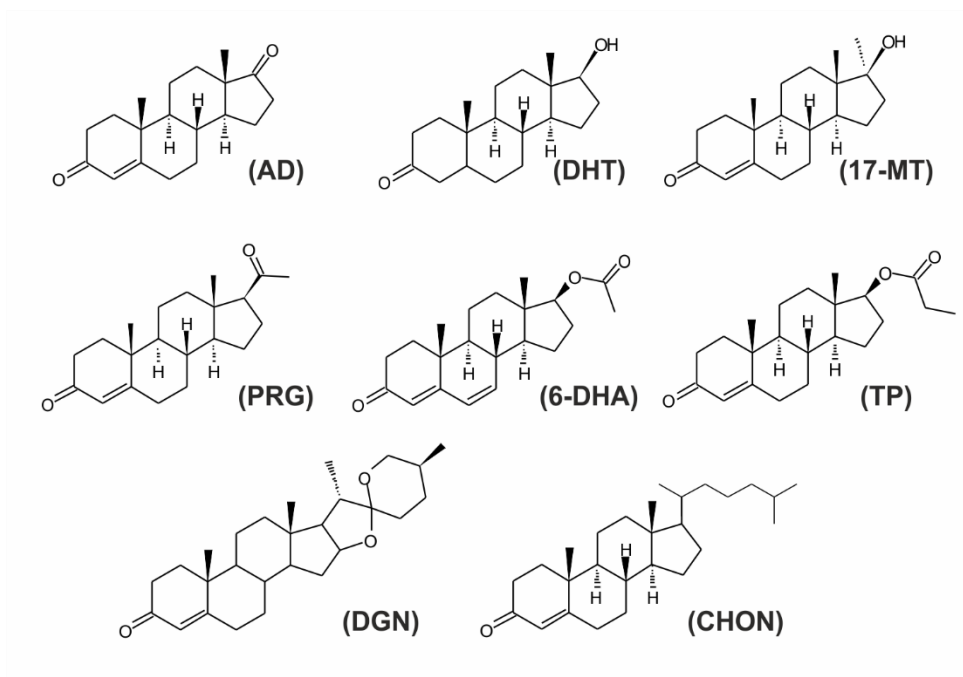
39

40 INTRODUCTION

41 Steroids belong to a class of lipid triterpenes characterized by a structure of an aliphatic
42 tetracyclic system with a low number of functional groups in its core, complex spatial structure,
43 and low solubility in water¹. They are widespread in plants, insects, vertebrates, yeasts, and
44 fungi². Cholesterol-derived steroids are used as hormones and regulate various aspects of the
45 metabolism. As a result, steroid hormones and their analogues are one of the most important
46 groups of drugs produced by the pharmaceutical industry³.

47 The chemical and biotechnological modification of steroids is of utmost importance for the
48 development of new functionalities of steroid drugs. One of such important modification is the
49 introduction of a double bond between the atoms C1 and C2 of ring A, so-called Δ^1 -
50 dehydrogenation, which increases the potency and selectivity of steroid drugs. For example, the
51 oxidation of hydrocortisone to prednisolone results in increased anti-inflammatory activity
52 while reducing salt-retaining activity^{4,5}. Δ^1 -Dehydrogenation, which starts the central
53 degradation pathway in bacteria (the opening of ring A leading to the complete mineralization
54 of the steroids), is catalysed by a microbial flavin enzyme, 3-ketosteroid Δ^1 -dehydrogenase
55 (KstD, EC 1.3.99.4). The genes encoding KstDs, characterized by a rather high sequence
56 diversity, are abundant among various bacteria and fungi⁶. As a result, microbial systems are
57 routinely used by the pharmaceutical industry in the biotransformation of various sterols and
58 steroids^{7,8}.

59



60
 61 Figure 1. Steroids used in the study; AD – androst-4-en-3,17-dione, DHT – dihydrotestosterone,
 62 17-MT – 17-methyltestosterone, PRG – progesterone, 6-DHA – 6-dehydrotestosterone acetate,
 63 TP – testosterone propionate, DGN – diosgenone, CHON – cholest-4-en-3-one.

64
 65 Steroid-transforming bacteria frequently have several isoenzymes at their disposal. These
 66 isoenzymes usually differ in their substrate preference and are up-regulated in the presence of
 67 different steroids⁶. Multiple isoenzymes in a genome may help microorganisms degrade
 68 steroids with different structural characteristics⁶. Recently, several reports confirmed that
 69 KstDs are capable of dehydrogenating steroids with undegraded isooctyl C17 substituents^{9,10}.
 70 One such non-standard KstDs is Acmb from *Sterolibacterium denitrificans* Chol-1, a suitable
 71 catalyst for the dehydrogenation of C17-extended ketosteroids and 3-keto-saponins.
 72 Interestingly, it also exhibits multiple pH optima, which depends on the electron acceptor used.
 73 As a result Acmb can catalyse the 1,2-dehydrogenation of 3-ketosteroids at a slightly acidic or
 74 basic pH^{11,12}.
 75 Furthermore, the sequence of Acmb also differs from the only structurally characterized
 76 representative of the KstDs, namely the KstD1 from *Rhodococcus erythropolis* (PDB: 4C3X

77 and 4C3Y)¹³. Our bioinformatic analysis indicates that KstD1 from *R. erythropolis* (GenBank
78 accession code AAF19054.1) is shorter by approximately 50 amino acids when compared to
79 the majority of the known KstD sequences. The longest difference in the amino acid sequence,
80 38 amino acids (compared to the sequence of Acmb, see Figure S1), was previously referred
81 to as the 'loop'¹⁰. As a result, the crystal structure of KstD1 from *R. erythropolis* represents only
82 a fraction of the known enzymes in the KstD family. In this work, we structurally characterize
83 KstD from *S. denitrificans* (Acmb, GenBank accession code ABV59992), which, based on its
84 amino acid sequence composition, represents most of the known KstDs. The structural
85 characterization is combined with kinetic and modelling studies addressing the reaction
86 mechanism with several steroid substrates (Figure 1). With pre-steady-state kinetics, we
87 explained the surprising origin of two pH optima of Acmb¹¹. We have also successfully used
88 site-directed mutagenesis and QM/MM MD calculations to quantitatively explain the influence
89 of active site residues on reaction kinetics. Finally, we discussed the biological role of the 'loop'.
90 We discuss its possible involvement in the enzyme-membrane association, the substrate
91 binding, and its potential responsibility for the substrate specificity of Acmb.

92 **METHODS**

93 **Materials**

94 All chemicals were purchased from Sigma-Aldrich, Tokyo Chemical Industry, Carl Roth or
95 BioShop unless otherwise specified. 2,2,4,6,6-d₅-4-Androsten-17 α -methyl-17 β -ol-3-one was
96 purchased from CDN Isotopes, while 1,16,16,17-d₄-17 β -hydroxy-5 α -androstan-3-one was
97 obtained from Alsachim.

98 **Protein purification and crystallization**

99 Acmb was expressed in *Escherichia coli* BL21(DE3)Magic (Creative Biolabs) and purified
100 by Ni-affinity chromatography as previously described by Wojtkiewicz *et al*¹¹. The removal of
101 (His)₆-Acmb fusion protein was carried out during overnight dialysis with recombinant (His)₆-
102 TEV protease. The protein was then loaded onto the HiLoad Superdex 200 16/600 pg (Cytiva)

103 size exclusion column and eluted with 50 mM Tris-HCl pH 8.5, 150 mM NaCl, 0.5 mM tris(2-
104 carboxyethyl)phosphine (TCEP) and 0.2% (v/v) Tween 20. All chromatographic experiments
105 were performed using an NGC Quest 10 Plus instrument (BioRad).

106 The protein was concentrated to 20 mg ml⁻¹ using an Amicon Ultra-15 30 kDa (Millipore)
107 and incubated on ice with the excess amount of androst-1,4-diene-3,17-dione (ADD) for
108 approximately 3 hours. Subsequently, the solution was centrifuged at 14 000 g, 4° C for 5
109 minutes. Crystallization conditions were screened using MCSG1, MCSG2, MCSG3, Top96,
110 SuperCOMBI, PurePEGs (Anatrace), Index, Silver Bullets, and PEG/Ion HT (Hampton
111 Research) with success in the MCSG1 screen. Crystallization experiments were performed
112 using the sitting-drop vapour diffusion method by mixing 1:1 screen solution with the protein
113 solution. Finally, a diffraction-quality crystal grew in 0.1 M HEPES NaOH pH 7.5, 25% (w/v)
114 PEG 3350 (MCSG1). For XRD experiments, the crystal was cryoprotected by drying over 1 M
115 NaCl and flash-cooled in liquid nitrogen.

116 **Data collection and analysis**

117 Initial crystallization and structure determination were performed in Minorlab with data
118 collected in Argonne. Later, a better crystal was used to obtain 1.84 Å diffraction data collected
119 at a temperature of 100 K on the BESSY 14.1 beamline (Helmholtz-Zentrum Berlin, Germany)
120 using a Dectris PILATUS 6M detector. The data set was recorded at a wavelength of 0.9184 Å.
121 Data were collected and processed using CrysAlis^{Pro}¹⁴ and XDS¹⁵. The structure solution and
122 model building were carried out with Phenix (AutoBuild)¹⁶ and CCP4 (ARP/wARP,
123 BUCCANEER)¹⁷. The structure was solved by molecular replacement with the structure of *R.*
124 *erythropolis* (PDB: 4C3Y)¹³ as a search model. The resulting model was then refined with
125 REFMAC 5.8¹⁸ and manually rebuilt with WinCOOT 0.8.9.2¹⁹. The quality of the model was
126 evaluated using Molprobity²⁰ and the wwPDB Validation Service²¹. The data were deposited

127 in the PDB with PDB code 7P18. The quality of diffraction data and structure refinement is
128 present in Table S3 (supplementary material).

129 The structure was further analysed using PyMOL²², Chimera 1.15²³, and Discovery Studio
130 2018²⁴. The membrane-associated region was predicted with Orientations of Protein in
131 Membranes database and PPM 3.0 using the bacterial Gram-negative inner membrane model²⁵.

132

133 **Site-directed mutagenesis**

134 The pMCSG7-acmb plasmid²⁶ was used as a template for site-directed mutagenesis introducing
135 point mutations (Y115F, Y118F, Y363F, Y467F, Y536F, G540P) into the Acmb gene. The
136 details of the procedure are available in SI. The FAD content in the expressed enzymes was
137 estimated as the ratio of the spectrophotometrically measured Acmb-FAD concentration (ϵ_{Acmb}
138 $_{450 \text{ nm}} = 12\,094 \text{ M}^{-1} \text{ cm}^{-1}$, determined as in²⁷) to the total protein concentration determined
139 according to the Bradford method¹⁴.

140 **Kinetic assays**

141 **Stopped-flow spectrophotometric activity assay**

142 The pre-steady state and steady-state kinetics aimed at establishing the kinetic mechanisms
143 of the enzyme were collected using a stopped-flow spectrophotometer SX20 (Applied
144 Photophysics). The solutions were treated with argon for several minutes to provide anaerobic
145 conditions. All reported concentrations are the final values obtained after mixing and diluting
146 the reactants. All measurements were performed in triplicate. Data were collected using Pro-
147 Data software and processed using OriginPro 2019b software.

148

149 **RHR and OHR pH optimum**

150 The pre-steady-state kinetics was used to determine the pH optimum of reductive half-reaction
151 (RHR) and oxidative half-reaction (OHR) catalysed by Acmb. The following buffers were

152 used: 50 mM Tris-HCl, 150 mM NaCl, 5% (w/v) glycerol (pH 7.5–8.5) and 50 mM glycine-
153 NaOH, 150 mM NaCl, 5% (w/v) glycerol (pH 9.0–10.0). The enzyme purified with Ni-affinity
154 chromatography¹¹ was transferred to the respective buffer using Econo-Pac® 10DG desalting
155 columns (BioRad) according to the instruction manual. Due to the rapid aggregation of the
156 enzyme at low pH observed under the concentration required for the stopped-flow experiment,
157 it was impossible to measure the reduction rate below pH 7.5.

158 For RHR, the FAD reduction was followed at 450 nm at 20°C in the reaction of 9.3 μM of
159 AcMB with 100 μM progesterone using the buffers described above. In each measurement, one
160 glass syringe of the stopped-flow instrument was filled with the solution of the steroid dissolved
161 in EGME (the final concentration of 8%) and buffer solution, while the second one contained
162 the enzyme solution in the buffer.

163 In the case of the OHR experiment, the enzyme was first reduced under anaerobic conditions
164 with a sub-equivalent amount of progesterone (1:0.8), thus avoiding the excess progesterone
165 that would interfere with the enzyme reoxidation. In each measurement, one glass syringe was
166 filled with the buffer solution of the reduced AcMB, and the second syringe was filled with the
167 buffer solution of 2,6-dichloroindophenol (DCPIP) and 2-methoxyethanol (EGME). The
168 solutions were treated with argon for several minutes before the experiment. The OHR reaction
169 was followed at 616 nm and 20°C in 50 μM DCPIP in 8% EGME with 10 μM AcMB in the
170 buffer solution. The obtained traces were fitted with double exponential functions yielding
171 eigenvalues λ_{obs} .

172 **Kinetic studies**

173 The steady-state kinetic studies leading to establishing the kinetic mechanism were conducted
174 with stopped-flow according to the previously described methodology²⁷. The reaction mixture
175 after mixing in stopped-flow contained 100 mM K₂HPO₄/KH₂PO₄ buffer pH 6.5, 52.2 nM of
176 AcMB with 50% FAD content, 1% isopropyl alcohol (IPA), and varying concentrations of

177 DCPIP (0.1–0.3 mM) and progesterone (2.5–50 μ M). In order to establish the kinetic
178 mechanism, the received data were fitted with nonlinear regression to three two-substrate
179 kinetic models (i.e., sequential ordered bi-bi and random sequential bi-bi and the nonsequential
180 Ping-Pong bi-bi models). The best model was selected based on statistical parameters (i.e., R^2 ,
181 χ^2 , AICc, and errors of estimated constants).

182

183 **Activity assay for mutated variants and kinetic isotope effect**

184 The kinetic assays of mutein activities, as well as steady-state values for the direct kinetic
185 isotope effect, were obtained using a UV-2700 spectrophotometer (Shimadzu) in 0.5 mL quartz
186 cuvettes with a 10 mm path. The reduction of DCPIP was followed at 700 nm ($\epsilon_{700[\text{pH } 6.5]} = 4$
187 $576 \text{ M}^{-1} \text{ cm}^{-1}$ or $\epsilon_{700[\text{pH } 8.5]} = 5\ 190 \text{ M}^{-1} \text{ cm}^{-1}$) at 30°C. kinetic curves' initial parts (5-10 s).

188 The specific activities of wild-type Acmb and its mutants were determined in the reaction
189 that consisted of 0.1 M $\text{KH}_2\text{PO}_4/\text{K}_2\text{HPO}_4$ buffer pH 6.5, 200 μ M DCPIP, 100 μ M androst-4-
190 en-3,17-dione (AD) in IPA (the final concentration of 2%) and 0.15 – 0.42 μ M of Acmb.

191 **HPLC activity assay**

192 Activities of muteins were additionally confirmed with HPLC analysis. The reaction mixture
193 consisted of 0.1 M $\text{KH}_2\text{PO}_4/\text{K}_2\text{HPO}_4$ buffer pH 6.5, 400 μ M DCPIP, 200 μ M AD in IPA (2%)
194 and 24.6 – 38.9 μ M of Acmb. The reactions were carried out in a thermoblock at 30° C and
195 800 rpm for 30 minutes. The reaction progress was stopped after 30 minutes by mixing the
196 samples with acetonitrile (1:1), followed by centrifugation at 14 000 g for 5 minutes and
197 analysis with LC DAD-HPLC (Agilent 1100) according to Wojtkiewicz et al.¹.

198 **Kinetic isotope effect**

199 The kinetic isotope effect (KIE) was determined with direct and competition methods. In the
200 direct approach, the reaction rates were determined in the spectrophotometric activity assay
201 described above. Measurements were carried out in 100 mM $\text{K}_2\text{HPO}_4/\text{KH}_2\text{PO}_4$ pH 6.5 or 50

202 mM Tris-HCl pH 8.5 with 200 μ M DCPIP, 100 μ M (pH 6.5) or 200 μ M (pH 8.5) steroid (17-
203 MT, 2,2,4,6,6-d₅-17-MT, DHT and 1,16,16,17-d₄-DHT) dissolved in dioxane (the final
204 concentration 1% or 2%, respectively) and 0.17 μ M of Acmb.

205 For the competitive kinetic isotope effect, $^D(V/K)$ was measured according to the previously
206 described protocol^{28,29}. The value of $^D(V/K)$ KIE was established based on the fractions of the
207 converted nondeuterated (x_1) and deuterated (x_2) substrate according to the formula:

$$208 \quad \left(\frac{V}{K}\right) = \frac{k_1}{k_2} = \frac{\log(1 - x_1)}{\log(1 - x_2)}$$

209 And KIE was established by a nonlinear fit to the reformulated function of $x_1(x_2)$:

$$210 \quad x_1 \log(1 - x_2)^{k_1/k_2}$$

211 The reaction mixtures consisted of 50 mM K₂HPO₄/KH₂PO₄ pH 6.5 or 50 mM Tris-HCl pH
212 8.5, 100 μ M DCPIP, equal 100 μ M amounts of substrates and their deuterated homologues (17-
213 MT and 2,2,4,6,6-d₅-17-MT or DHT and 1,16,16,17-d₄-DHT) in EGME (the final
214 concentration 2%), and Acmb (1.9 nM for pH 6.5 or 4.7 nM for pH 8.5). The reactions were
215 carried out in triplicate under anaerobic conditions [98:2 (v/v) N₂/H₂] at 30° C for 18 min. The
216 conversion of each substrate was analysed with LC-ESI-MS/MS (Agilent 1290 Infinity System
217 equipped with an MS Agilent 6460 Triple Quad Detector). The separation was conducted on
218 the Zorbax Eclipse Plus C18 column (1.8 μ m, 2.1 \times 50 mm, Agilent Technologies) In the
219 isocratic mode using ACN/H₂O/HCOOH (60:40:0.1 (v/v/v)) mobile phase at 0.4 ml/min flow
220 rate. The MS signals were collected in the positive single-ion monitoring mode (303.3, 308.3,
221 301.3, and 305.3 m/z signals for [M + H]⁺ of 17-MT, 2,2,4,6,6-d₅-17-MT, methandienone
222 (MTD), and 2,4,6,6-d₄-MTD, respectively as well as 291.3, 295.3, 289.3, and 292.3 m/z for [M
223 + H]⁺ of DHT, 1,16,16,17-d₄-DHT, 1-testosterone (1-TE), and 16,16,17-d₃-1-TE, respectively)
224 see Supporting Information, Table S1 and Figure S2. The quantitation of analytes was
225 conducted according to a previously established protocol.

226

227 **Bioinformatics and Computational**

228 **Phylogenetic tree**

229 For template sequences: KstD1 (WP_020909157) from *R. erythropolis* SQ1, Acmb
230 (WP_154715887) and Acmb2 (WP_067169324) from *S. denitrificans* Chol-1 we run protein
231 blast using Protein BLAST algorithm (NCBI) for 5000 hits. From alignment, we selected
232 sequences with >90% query cover and >30% identity from different microorganisms. Selected
233 sequences together with templates (81 sequences in total) were further aligned using Multiple
234 Sequence Alignment (Clustal Omega)³⁰. Obtained phylogenetic tree was visualized using
235 FigTree v1.4.4. The sequence alignment was analysed with Jalview³¹.

236 **Models setup**

237 The structure of chain A of Acmb in complex with the reaction product (androst-1,4-diene-
238 3,17-dione, ADD) available in the PDB (code 7P18) was used to prepare the model for further
239 simulations. ADD was replaced by other ketosteroids, i.e., AD, 17-methyltestosterone (17-MT)
240 or dihydrotestosterone (DHT), with the use of the Kabsch algorithm³². The protonation states
241 of the titrable amino acids were determined with propKa3.1^{33,34} for pH 6.5. The missing
242 molecular mechanics (MM) charges for ketosteroids were obtained with Gaussian16³⁵ at the
243 B3LYP/6-31G(d,p) level of theory³⁶. The FAD parameters were taken from RESP ESP charge
244 DataBase (R.E.DD.B)³⁷. The charge of the protein, ketosteroid, and FAD combined was +1,
245 which was neutralized by the addition of one Cl⁻ ion. The models were soaked with TIP3P
246 water molecules in a 94.4 × 78.8 × 78.4 Å³ box.

247 **Molecular dynamics simulations**

248 For all MD simulations, the Amber package with ff03 forcefield was used^{38,39}. Each model
249 was first optimized and then heated from 0 to 303 K with the NVT ensemble. Then 100 ps with
250 NPT conditions were simulated to equilibrate the system. Finally, 60 nanoseconds of molecular

251 dynamics simulation with periodic boundary conditions, controlled with a Langevin thermostat
252 were conducted. A cutoff for nonbonding interactions was set to 8.0 Å.

253 **Binding Free Energy and Interaction Energy**

254 The MM-PBSA algorithm⁴⁰ was used to estimate the change of Gibbs free energy of
255 substrate binding (ΔG_b). From each trajectory, two ΔG_b estimates were received: total ΔG_b for
256 the whole simulation and ΔG_{best} estimated for the 5 nanoseconds simulation with the best
257 geometry parameters of the bound substrate. These results were compared with MM-PBSA
258 analysis of enzyme: substrate MD simulations of KstD1 from *R. erythropolis*¹², which were
259 analysed according to the above protocol.

260 Average interaction energies between the ligand and each amino acid of AcmB were
261 calculated for the MD simulation fragment related to ΔG_{best} . Interaction energies were computed
262 as the difference between the energy of the ligand-amino acid pair and the sum of energies for
263 the separated ligand and residue.

264

265 **QM/MM MD simulations**

266 QM/MM modelling was performed with three different substrates: AD, 17-MT, and DHT.
267 The first one was used not only with wild type of AcmB but also with mutants (Y118F, Y115F,
268 Y467F, Y536F) in order to match the kinetic experiments (Figure S3). All of the models were
269 treated according to the procedure described below.

270 The QM layer consisted of the steroid substrate, Y363, and the FAD fragment (similarly to
271 our last study²⁷), while other residues were treated with the AMBER forcefield as implemented
272 in fDynamo library^{41,42}. The positions of residues beyond 20 Å from the substrate were fixed.
273 Two antisymmetric combinations of distances were selected as reaction coordinates to describe
274 the transfer of both hydrogen atoms: rC2H-rOH (proton abstraction) and rC1H-rNH (hydride
275 transfer). One-dimensional potential energy scans were performed to generate the initial

276 structures for QM/MM MD simulations. The reaction was studied with the umbrella sampling
277 method⁴³, at each window of simulation a parabolic penalty potential was added with a force
278 constant of 2500 kJ/Å² mol. One QM/MM MD simulation consisted of 5 ps of system
279 relaxation, and then 20 ps of simulation, results of which were used for further analysis. The
280 weighted histogram analysis method⁴⁴ was used to combine the QM/MM MD results into a
281 distribution function. QM/MM MD simulations were run at the AM1/AMBER level of theory⁴⁵.
282 The obtained profiles were corrected with the energy spline function defined in terms of
283 interpolated corrections⁴⁶⁻⁴⁸. Single point calculations were performed at B3LYP/6-
284 311++G(2d,2p)/AMBER level of theory, for geometries used for initial structures for QM/MM
285 MD simulations. After that, stationary state structures were optimized with the Baker
286 algorithm⁴⁹ and using the micro-macro iteration scheme⁵⁰ at AM1/AMBER and B3LYP/6-
287 31G(d,p)/AMBER levels of theory. Every optimized structure was verified by calculating the
288 Hessian and checking the number of imaginary frequencies. Kinetic isotope effects (KIEs) for
289 DHT and 17-MT were calculated from the definition of the free energy of a state⁵¹. For each of
290 the stationary states, E:S, TS1, E:I, and TS2, three structures were optimized. Then KIEs for
291 every elementary step were calculated as described elsewhere^{52,53}.

292

293 **RESULTS**

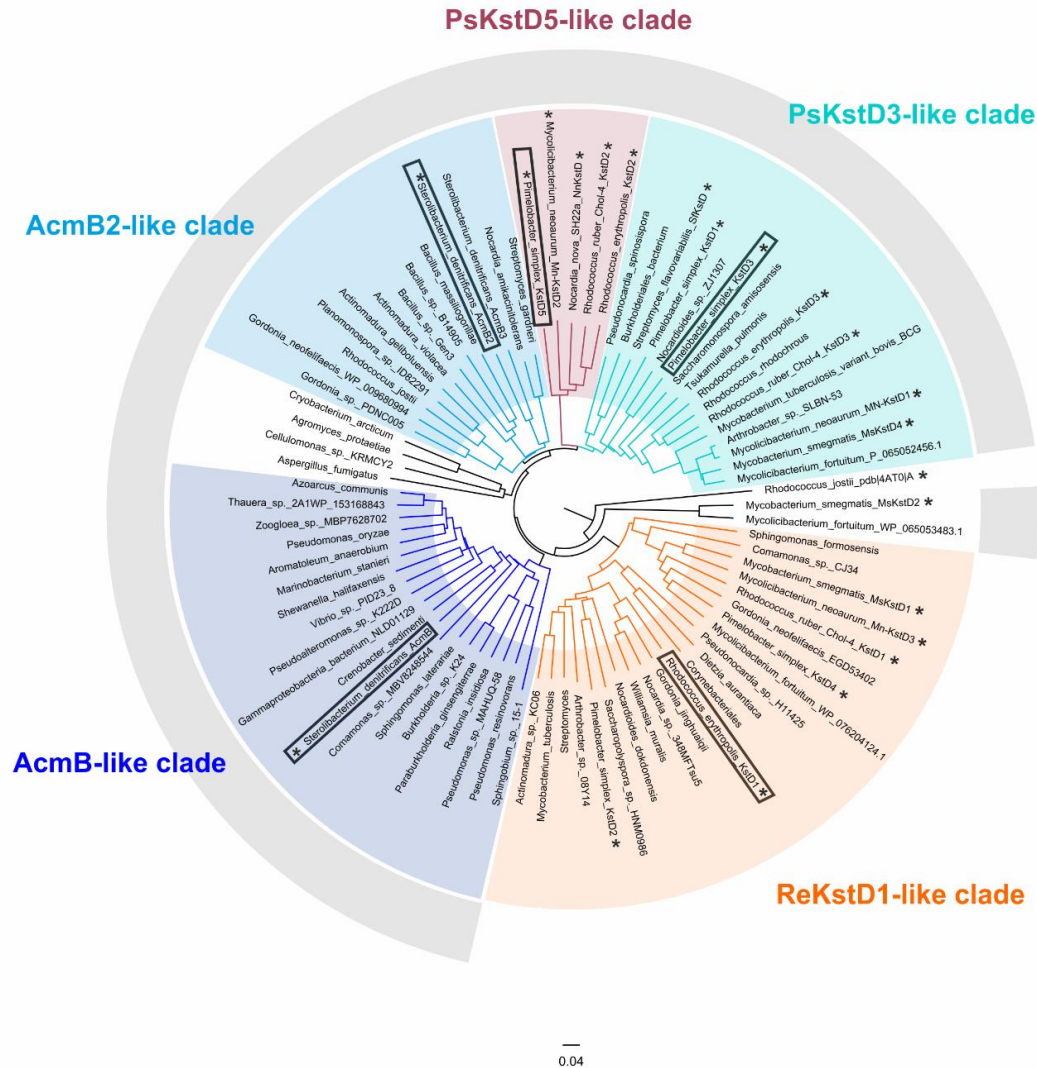
294 **Bioinformatic analysis**

295 We have performed an exhaustive analysis of KstD sequences based on multiple sequence
296 alignment. We selected 83 sequences from a diverse set of organisms from over 5000 retrieved
297 sequences that exhibited >90% query cover and >30% identity with respect to KstD1
298 (WP_020909157) from *R. erythropolis* SQ1, AcmbB (WP_154715887), and AcmbB2
299 (WP_067169324) from *S. denitrificans* (see Supplementary Information). The phylogenetic
300 analysis showed that the analysed sequences can be divided into five general clades, which we

301 named after representative KstDs with characterized substrate specificity such as ReKstD1-like
302 from *R. erythropolis*, PsKstD3-like, PsKstD4-like from *Pimelobacter simplex*, and finally
303 AcmbB-like and AcmbB2-like from *S. denitrificans* (Figure S4, Table S2).

304 KstDs with shorter sequences lacking the 'loop' aggregated solely into ReKstD1-like clade
305 which contained mostly actinobacteria such as KstD from *Mycobacterium* spp.⁵⁴, KstD1 from
306 *R. ruber* Chol-4⁵⁵, and *P. simplex* KstD2, and KstD4¹⁰. The two clades represented by *P.*
307 *simplex*, PsKstD3-like and PsKstD5-like, contained several well-characterized
308 dehydrogenases, such as KstD4 from *M. smegmatis*⁵⁶, and several enzymes from *Rhodococcus*
309 spp., *P. simplex*, *Streptomyces flavovariabilis* and *Nocardia nova*. Both clades were composed
310 of KstDs from actinobacteria with rare examples of proteobacteria. Meanwhile, in clades
311 AcmbB- and AcmbB2-like we could not identify any other biochemically characterized enzymes.
312 The AcmbB-like clade was mostly composed of sequences from proteobacteria, while in the case
313 of the AcmbB2-like clade, we identified numerous members of actinobacteria and less numerous
314 firmicutes and proteobacteria. Interestingly, the KstD2 from *Mycobacterium smegmatis* was
315 classified as a phylogenetically different sequence indicating the existence of yet another
316 phylogenetic clade that was not represented by our selection of sequences.

317 Remarkably, if the same analysis is conducted only for the 'loop' region, we obtain a very
318 similar phylogenetic tree (Figure S4). This indicates that the loop region is an important
319 determinant of KstDs sequence diversity.



320
 321 Figure 2. Phylogenetic analysis of the KstDs from *Sterolibacterium denitrificans* and
 322 representative orthologues in other species. The tree was rooted to Δ^4 -KstD from *Rhodococcus*
 323 *josti*⁵⁷. The scale length was set as 0.04; the asterisk marks enzymes with identified activity;
 324 KstDs in frames indicate enzymes representative of the clade with characterized structure or
 325 substrate specificity. Gray rim indicates sequences with an additional 'loop'.

326 Acmb crystal structure

327 In the course of the crystallization experiments, a single yellow crystal of wild-type Acmb
 328 was obtained in trigonal form with two molecules in the asymmetric unit (ASU), denoted as
 329 chains A and B in the PDB structure. Although a few hydrogen bonding interactions exist

330 between the molecules, the size exclusion chromatography experiments and atomic force
331 microscopy imaging²⁶ showed that AcnB occurs as a monomer in solution (Figure S5). The
332 high similarity of monomers A and B was proved by the low value of r.m.s deviations for C α
333 atoms (0.174 Å). The subtle differences between chains A and B are correlated with the
334 different number of bound ligands. Analysis of the crystal structure proved that a FAD molecule
335 is present in both monomers, while an ADD ligand occupies the active site of molecule A. The
336 electron density maps have very good quality for almost the entire protein molecules, except
337 for short disordered regions at the N-terminus of both monomers (MSI of A and MSIE of B),
338 as well as for side chains of a few residues (L194A, M180B, L194B and L198B). Those regions
339 were excluded from the refinement. Data collection and refinement statistics are summarized
340 in Table S3.

341 **Overall structure**

342 The AcnB has an α/β fold formed by three tightly packed domains. The molecule has an
343 elongated shape with dimensions of 52 x 55 x 72 Å³, its volume equals 69445 Å³ and a surface
344 area of 21035 Å². The overall architecture is very similar to KstD1 with a RMS deviation of
345 0.927 Å calculated for C α . The largest, FAD-binding domain comprises helices H2–H5, H10–
346 H13 and H21–H22 (Figure 3A). This domain also contains three β -sheets: the largest one,
347 antiparallel β -sheet A (B1–B2, B10–B13 and B23), antiparallel β -sheet B (B3–B5) and small
348 two-stranded β -sheet E (B14–B21). The second catalytic domain (A320–T498) consists of a
349 six-stranded antiparallel β -sheet F (strands B15–B20) located in the core of the molecule
350 decorated with seven helices (H14–H20). The third domain (Y153–R204) comprises a unique
351 part, not observed in the KstD1 structure, which we believe serves as a region responsible for
352 the association of the enzyme to the cell membrane.

353 **Putative membrane-associated domain**

354 Initially, we expected that the fragment Y153–R204 would be disordered since this region is
355 missing in homologous proteins of microbial origin and our homologous modelling did not
356 predict any secondary structure elements in the long loop²⁶. However, our structural data
357 showed for the first time that the domain Y153–R204 of AcmB not only forms secondary
358 structures but also closes around the product, further tightening its binding (Figure 3E). The
359 domain is composed of four helices (H6–H9) together with an antiparallel β -sheet D (B7–B8).
360 The hypothesis on the function of this domain was corroborated by the prediction of membrane-
361 embedded residues of 178–198 (H8 and H9) by the PPM 3.0 server (Figures 3C and S6). The
362 predictor classified AcmB as a peripheral protein with $\Delta G_{\text{transfer}}$ of -12 kcal/mol. This important
363 difference from KstD1 may also result in the concomitant stabilization of the ligands (see
364 below). As a result, we named the Y153–R204 fragment the putative membrane-associated
365 domain.

366 AcmB is an amphipathic protein located in the cytoplasm or periplasmic space, and it binds
367 to the cytoplasmic membrane through weak dispersion interactions^{9,26}. We also observed a high
368 aggregation tendency of AcmB, which was not reported in the case of KstD1²⁶. Thus, it could
369 be hypothesized that an additional domain is responsible for anchoring the protein to the
370 bacterial cytoplasmic membrane. Probably, the binding of the protein to the membrane occurs
371 through a longer amphipathic α -helix (H9) (Figure S5A). Since helix H9 is parallel to the lipid
372 bilayer, its hydrophobic part is separated from the water environment, whereas the polar surface
373 of the helix interacts with the water phase and negatively charged phosphoryl groups, the
374 membrane-associated domain can penetrate the area of polar bilayer groups. Such an orientation
375 of the enzyme would also locate the active site near the membrane allowing steroids to dissolve
376 in it. The association of proteins with the membrane is quite common among steroid-
377 transforming enzymes such as cholesterol oxidase⁵⁸.

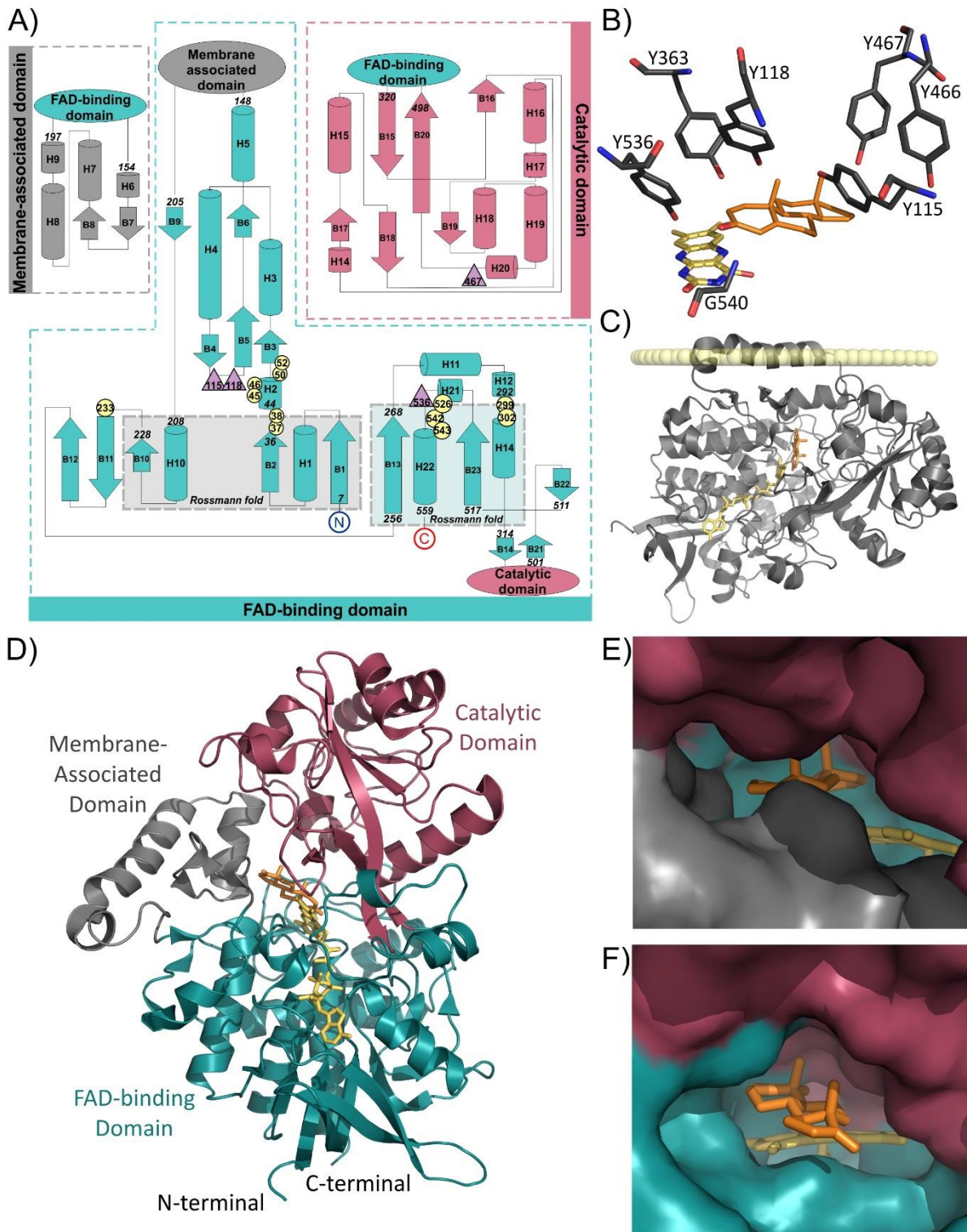
378 Furthermore, the analysis of the B factors and our MD modelling showed that the membrane-
379 associated domain is the most flexible and mobile element of the structure of AcmB (Figures
380 S6B and S7). These facts indicate that this domain or a part of it could function as a lid that
381 closes the active site after the substrate binds to the protein. However, unequivocal confirmation
382 of this hypothesis would require the determination of apo-enzyme structure.

383
384 To better understand the role of the unique domain Y153–R204, the surface of the protein was
385 analysed in terms of its electrostatic potential. In Figure S8, the surface of AcmB is shown with
386 the positively charged amino acids (arginine, lysine, and histidine) marked in blue, and the
387 negatively charged amino acid residues (aspartic acid, glutamic acid) are coloured red. The
388 highest concentration of positively charged amino acids is observed within the putative
389 membrane-associated domain (marked with a black dashed line). This observation further
390 supports the suggested role of domain Y153–T204 in the interaction with the lipid bilayer of
391 membranes.

392 **FAD-binding Site**

393 The FAD-binding domain comprises regions E4–A152, K205–W319, and K499–K561 (Figure
394 3A) and presents a conserved fold previously observed in KstD1. The main part of the FAD-
395 binding domain adopts the super-secondary structure, the characteristic of the Rossmann fold
396 (Figure S9). Its arrangement differs from a basic topology and it is a typical variation of the
397 fold noticed for dehydrogenases⁵⁹. The fold that binds dinucleotides such as FAD involves two
398 Rossmann binding motifs, which typically form a six-stranded parallel β -sheet flanked by α -
399 helices. As was observed in KstD1, the first half of the Rossmann fold in AcmB (B1-H1-B2-
400 B10-B10) is very similar to the basic topology, while the second half (B13-B13-B23-H22) is
401 slightly different from the basic arrangements since the third β -strand is not present. Besides
402 the missing β -strand, the variation of the fold observed for dehydrogenases includes a three-
403 stranded β -meander (B11-B12 and part of B13) connecting two halves of the Rossmann fold,

404 instead of the crossover α -helix, as in AcmB structure. In addition to the Rossmann fold, the
 405 FAD-binding domain is decorated with several secondary structure elements.
 406



407
 408 **Figure 3. A) Topology of AcmB chain A and its overall structure;** residues involved in FAD
 409 coordination are marked as yellow circles, residues involved in catalysis are marked by purple

410 triangles; B) Acmb active site with catalytically crucial residues, FAD in yellow, ADD in
411 orange; C) alignment of Acmb at the membrane; D) overall fold of Acmb molecule with FAD-
412 binding domain (green), putative membrane-associated domain (grey) and catalytic domain
413 (red); E) entrance to Acmb active site, and F) entrance to the active site of KstD1.

414
415

416 Due to the numerous insertions within the previously described Rossmann motif (especially
417 between B2 and H10), it can be concluded that Acmb belongs to the GR2 subfamily of the
418 structural family of glutathione reductase (GR). The aforementioned insertions make alignment
419 of the amino acid sequence possible only for the first 30 amino acid residues from the N-
420 terminus. The most conserved structural motif of the GR family is the sequence
421 xhxhGxGxxGxxxhxxh(x)shxhE(D) (where x is any amino acid and h is a hydrophobic amino
422 acid), which is part of the Rossmann fold and located at the N-terminal part of the protein⁵⁹.

423 The main differences between the basic version of the analysed fragment and both known KstD
424 structures are the presence of alanine residue instead of glycine residue at the position of the
425 third conserved glycine and the number of amino acids between the two hydrophobic amino
426 acids in the final part of the sequence, which is seven for Acmb
427 (xhxhGxGxxAxxxhxxh(x)shxhE(D): ¹⁰VIVVGSAGAMLAAARAHDLGLSVLVVE³⁷).

428 This fragment forms the initial region of the Rossmann motif (B1-H1-B2) (Figure S9). There
429 are hydrophobic interactions between α -helix and β -sheets. The negatively charged, conserved
430 glutamic acid residue that terminates the motif (E37) forms hydrogen bonds with the hydroxyl
431 groups of adenosine monophosphate ribose. The FAD coenzyme in an extended conformation
432 occupies the elongated cavity of the largest domain (Figure 3D and S10A). The adenine end of
433 the cofactor reaches the floor of the cavity formed by H13, B2, and B11. The planar
434 isoalloxazine ring binds at the edge of the FAD-binding domain and reaches the catalytic
435 domain. Similar to the position revealed by the KstD1 structure, the isoalloxazine ring interacts
436 with the H2/B3 loop of the FAD-binding domain and the catalytic domain. The observed yellow
437 colour of the crystals suggests the presence of noncovalently bound FAD in an oxidized state.

438 The FAD molecule is stabilized at the active site by a network of hydrogen bonds formed by
439 residues: E37, K38, T45, S46, G50, A52, F233, N299, D302, N526, T542, and L543, as shown
440 in Figure S10A. Analysis of Acmb-FAD interactions also reveals numerous interactions of the
441 π -alkyl (V13, K38, I496, F338), π -sigma (A270, L543), and alkyl-alkyl (A294, I496).

442

443 **The active site of Acmb**

444 The active site of the Acmb binds the flavin part of the FAD and the 3-ketosteroid (here ADD
445 product) and is located in the area of contact of all three domains. Figure S10 shows that most
446 of the amino acids surrounding ADD are non-polar. The axial methyl groups on C10 and C13
447 carbons face the catalytic domain, and the sterane A ring is almost parallel to isoalloxazine
448 (Figure 3B). The active site contains six conserved tyrosine residues: Y115, Y118, and Y536
449 from the FAD-binding domain as well as Y363, Y466, and Y467 from the catalytic domain.
450 Similar to the active site of KstD1 from *R. erythropolis*, Y363 is positioned close to the C2
451 atom of the steroid, and we assume it is in the tyrosyl anion form. In this form, it can act as a
452 catalytic base during substrate activation (see below). Y363 is accompanied by Y118, which,
453 based on the short distance of their tyrosyl O atoms (2.8Å), forms an H-bond with Y363. The
454 Y536 hydroxyl and the G540 NH of the peptide bond form hydrogen bonds with carbonyl
455 oxygen at carbon C3 of ADD (Figure 3B). Additionally, the steroid core forms π -alkyl or alkyl-
456 alkyl interactions with the amino acids A52, F338, Y363, and A539.

457 These three tyrosines (Y363, Y118, and Y536) are directly involved in catalysis and are
458 connected via water (HOH701) with a proton relay system composed of Y115, Y467, and
459 Y466. Our bioinformatic analysis showed that these six tyrosines are highly conserved in the
460 majority of the analysed KstD sequences (65%), while the second most common motif consists
461 of only catalytic tyrosines (Y118, Y367, and Y536) encountered in 24% of the 82 analysed
462 sequences (Figure S3 and Table S2). This type of active site organization without an extended
463 proton relay system is present in the other known structure of KstD1 (Figure S11).

464 **AcmB kinetic mechanism**

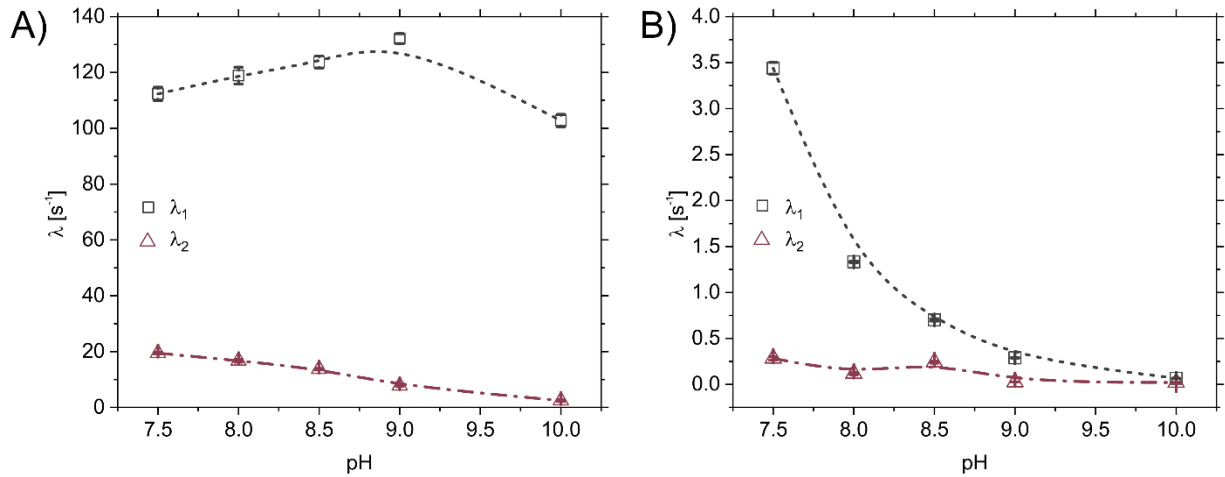
465 Kinetic experiments have confirmed that the reaction catalysed by AcmB proceeds according
466 to Ping-Pong bi-bi mechanisms, as recently reported by us for KstD1 from *R. erythropolis*²⁷.
467 AcmB exhibited a high affinity for progesterone with K_{mA} value of $4.4 \pm 0.3 \mu\text{M}$ and a 20-fold
468 lower affinity for DCPIP (K_{mB} $79.3 \pm 6.9 \mu\text{M}$). These data are consistent with the apparent
469 kinetic parameters reported previously¹¹. The established V_{\max} of the enzyme was $33.4 \pm 1 \mu\text{M}$
470 min^{-1} , which corresponds to k_{cat} of 21.3 s^{-1} .

471 **pH optimum of the half-reactions**

472 Under the Ping-Pong bi-bi mechanism, it is possible to independently study the kinetics of
473 reductive half-reaction (RHR), i.e., binding of the steroid substrate to the enzyme active site,
474 oxidation and reduction of the enzyme's FAD followed by the release of the product, and
475 oxidative half-reaction (OHR), i.e., binding of DCPIP to the active site, oxidation of FADH^- to
476 FAD and release of the reduced DCPIPH_2 . Therefore, we employed pre-steady-state kinetics to
477 investigate the pH dependence of both RHR and OHR. The aim was to explain our previous
478 observation that the enzyme exhibits two reaction pH optima; one at pH 6.5 when the reaction
479 was conducted with DCPIP and the second at pH 8.5 when the reaction was conducted with
480 PMS or PMS and DCPIP¹¹. Initially, we hypothesized that under acidic conditions, the reaction
481 catalysed by AcmB might proceed according to a different mechanism from that of the other
482 KstDs. However, later on, we suspected that it is the sluggish OHR that is responsible for the
483 observed pH optimum of the steady-state reaction.

484 To test that, we have examined the pH dependence of RHR and OHR in the range of 7.5–
485 10.0. The kinetic curves were fitted with a double exponential model yielding two eigenvalues
486 λ_1 and λ_2 (Figure 4). For the RHR, the λ_1 was in the range of 100 to 130 s^{-1} with a slight optimum
487 at pH 9.0, while λ_2 was in the range of 0– 20 s^{-1} and was linearly decreasing from pH 7.5 to
488 10.0. In the OHR reaction with DCPIP, the observed eigenvalues were much lower than those

489 observed for RHR and the highest λ_1 was observed at 7.5, indicating the pH optimum at lower
490 pH values, which were unfortunately beyond the experimentally accessible range due to the
491 rapid aggregation of the enzyme.



492

Figure 4. pH optima of A) reductive half-reaction (RHR, Acmb^{ox}+AD) and B) oxidative half-reaction (OHR, Acmb^{red}+DCPIP) of Acmb obtained in pre-steady-state kinetics. λ_1 and λ_2 represent eigenvalues of the double exponential model used to fit the observed kinetics. The error bars represent the standard deviation of the experiment.

493

494 **Substrate specificity**

495 Recently we have reported that the kinetics of Acmb point to cholest-4-en-3-one (CHON) as
496 a native substrate¹². Acmb differs from KstD1 by the presence of a 40 amino acid fragment
497 (153–204) that was formerly referred to as a 'loop' but that in fact, forms a putative membrane-
498 associated domain at the entrance of the active site (Figures 3E and F). Besides anchoring
499 Acmb to the membrane and positioning the active site entrance toward it, this domain seems to
500 be involved in the binding of substrates with extended C17 substituents, which stick out of the
501 KstD1 active site. We assume that the presence of this fragment may be responsible for the
502 unique substrate specificity of Acmb with respect to enzymes devoid of this sequence. To check
503 this hypothesis, we decided to conduct a series of MD simulations and estimate the free energy
504 of binding for Acmb:steroid complexes, as well as calculate the interaction energies of
505 substrates with the whole protein and membrane-associated domain (Table 1).

506 Theoretical predictions of ΔG_b obtained for Acmb turned out to be similar to those published
507 for KstD1¹² (Table S4–S6). The estimated free energy of binding for the effective enzyme-
508 substrate complexes (ΔG) for all analysed substrates ranged between -10 and -3.4 kcal/mol
509 (Table S4), but the ΔG s of the substrates with a degraded C17 substituent were in the range of
510 -7.6 to -3.7 kcal/mol. The best-bound substrate turned out to be cholest-4-en-3-one (-10
511 kcal/mol), while diosgenone was bound only with ΔG of -3.4 kcal/mol. The ΔG_{best} calculated
512 for the 5 nanoseconds of the best **E:S** geometries led to similar conclusions (range from -8.7 to
513 -6.1 kcal/mol, -12.4 kcal/mol for CHON). The analogical analysis conducted for the KstD1
514 from *R. erythropolis* yielded values of ΔG_b in the range of -9.3 to -3.8 kcal/mol. Cholest-4-en-
515 3-one was not different from other substrates (ΔG_b of -6.3 kcal/mol), but diosgenon exhibited
516 better stabilization than for Acmb (-5.8 kcal/mol). These results confirm the preferential
517 binding of cholest-4-en-3-one by the enzyme with an additional 'loop' and explain the better
518 apparent activity of KstD1 with diosgenone compared to Acmb¹². This result also suggests that
519 the membrane-associated domain plays a role in the differentiation of substrates with extended
520 C17 substituent (i.e., preferential binding of CHON over DSG).

521 Similarly, substrates with short C17 substituents had average interaction energy with
522 membrane-associated domain in the range of -11.1 to -4.5 kcal/mol, while for cholest-4-en-3-
523 one and diosgenone -15.7 and -13.5 kcal/mol, respectively (Figure S12). Accordingly, the
524 interaction with the whole protein was in the range of -53 to -40 kcal/mol, except for cholest-
525 4-en-3-one and diosgenone, for which it was approximately -60 kcal/mol. Closer analysis
526 indicates that the beginning of the membrane-associated domain is primarily responsible for
527 the stabilization of the substrates. The T156 universally stabilizes both smaller and bigger
528 substrates, while the hydrophobic residues between M164 and A169 are involved in the
529 stabilization of substrates with extended C17 substituents. These results suggest that the

530 membrane-associated domain is involved in the stabilization of the enzyme complexes with
 531 bigger substrates.

532

533 **Table 1** The estimated free energy of the binding (ΔG_b) of ketosteroids to the Acmb active site
 534 and average interaction energies (IE) between different substrates and Acmb or the membrane-
 535 associated.

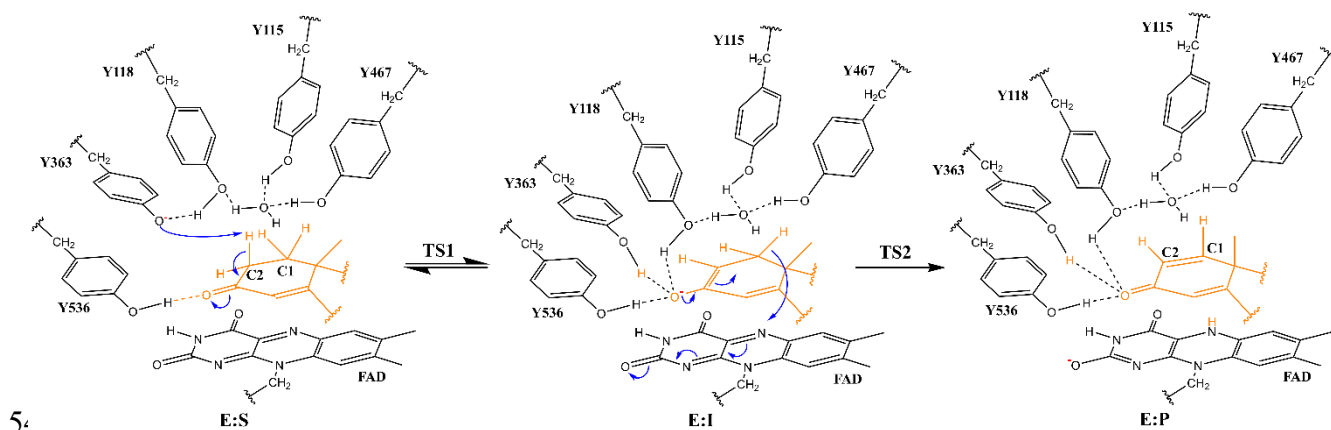
Substrate	Total ΔG_b [kcal/mol]	ΔG_{best} [kcal/mol]	IE [kcal/mol]	IE with res. 153–204 [kcal/mol]
Androst-4-en-3,17- dione (AD)	-4.1±0.2	-6.1 ± 0.1	-40.1±0.2	-4.93±0.05
Cholest-4-en-3-one (CHON)	-10.0 ± 0.3	-12.4± 0.1	-61.4±0.2	-15.68±0.08
Dihydrotestosterone (DHT)	-6.6±0.1	-7.0±0.1	-41.9±0.1	-10.63±0.06
Progesterone (PRG)	-6.3±0.2	-7.3±0.1	-42.0±0.2	-7.95±0.04
17-methyltestosterone (17-MT)	-7.6±0.1	-8.7±0.1	-46.3±0.2	-4.53±0.04
Testosterone propionate (TP)	-4.9±0.3	-7.1±0.1	-49.2±0.2	-10.02±0.07
6-Dehydrotestosterone acetate (6-DHA)	-3.8±0.5	-7.2±0.1	-53.4±0.2	-11.10±0.07
Diosgenone (DGN)	-3.4±0.3	-5.7±0.2	-60.0±0.2	-13.48±0.07

536

537 The most important interaction inside the binding site (Figure S13) is between the 3-keto
 538 group of the substrates and Y536 and G540, which form H-bond interactions (i.e., in the range
 539 of -6.4 to -2.4 kcal/mol) as well as via hydrophobic interactions F338 and A539. Interestingly,
 540 due to the lack of a double bond in ring A and the different position of the 3-keto group, DHT
 541 exhibits a different binding pattern, forming effective H-bond interaction only with G540 (IE
 542 -3.24 kcal/mol). The distance between the C3=O atom and H atom of the Y536 hydroxy

543 group is significantly longer in the case of DHT compared to the native substrate CHON
544 (median of 3.48 Å vs 2.94 Å, respectively).

545
546 **Reaction mechanism**



548 Figure 5. The scheme of mechanism for the reaction catalysed by Acmb.

549 The modelling revealed that the reaction mechanism catalysed by Acmb proceeds according
550 to the classical mechanism postulated in the literature and was recently confirmed by our
551 calculations for KstD1 from *R. erythropolis*²⁷ (Figure 5). The enzyme binds a steroid substrate
552 (E:S) so its ring A is positioned almost parallel to the isoalloxazine ring system of FAD. Y536
553 and G540 form H-bond interactions with the 3-keto group of the substrate, while the
554 deprotonated Y363 is positioned in close vicinity (1.9–2.2 Å) to the 2βH atom, prepared to
555 deprotonate the substrate (Figs. S13). Y363 forms a direct H-bond interaction with Y118, which
556 seems to be stabilizing its tyrosyl form. The Y363–Y118 tandem is connected via water to four
557 other tyrosines (Y115, Y463, Y466, and Y467) that provide H-bonding interactions for several
558 water molecules (Figure S14). These tyrosines, together with water molecules, form a proton
559 relay that enables the proton's swift transfer from the active site to the solvent. The water
560 molecule connecting the Y363–Y118 tandem with the proton relay system is not only present
561 in the crystal structure (HOH701 in chain A) but its position is also stable during most of the
562 MD simulations.

563 In the first step of the reaction (**TS1**), the hydrogen atom from the C2 position is abstracted
564 by a tyrosyl anion (Y363), which results in the formation of an enolate intermediate product
565 **E:I**, as indicated by the shortening of the C2–C3 bond from 1.5Å in **E:S** to 1.38Å in **E:I**. At
566 this point, the hydrogen bond network reorganizes, as Y363 and Y118 join the Y536 in H-bond
567 stabilization of the negative charge at the 3-keto group of the steroid enolate. In the second step
568 (**TS2**), a hydride anion from the 1 α C position is transferred to the N5 atom of FAD yielding
569 reduced FADH⁻ and 1-dehydro product (**E:P**). The stationary states of the pathway are
570 presented in Figure S15.

571 As in our previous calculations for KstD1²⁷, both barriers are of similar height (13.5 and 15.6
572 kcal/mol), with **TS1** slightly lower (2.3 kcal/mol) than **TS2** (Table 2, Figure S18). The **E:I** is
573 very well stabilized (2.7 kcal/mol), and the final product **E:P** is exergonic (-9.2 kcal/mol).

574 The modelling showed that the energy profile for AD is very similar to that of 17-MT (Figure
575 S20). This was expected because the only structural difference between AD and 17-MT
576 (substitution of C17) is pointed toward the entrance to the active site (Figure S16). However,
577 in the case of DHT, which has no double bond in ring A, we observed an elevation of both
578 barriers and energy of **E:I** by approx. 3 kcal/mol. The saturated A ring of the substrate results
579 in a slightly later **TS1** and an earlier **TS2** compared to the geometries obtained with AD (Figures
580 S17 and S20) and higher charge separation in the **E:I**. These results are consistent with our
581 steady-state kinetic experiments, which yielded respectively 71% and 19% specific activity of
582 Acmb with 17-MT and DHT with respect to AD (Table 2). Interestingly, we obtained the best
583 PES for Acmb native substrate (Fig. S20), CHON. The C-H activation was very similar to AD
584 (Fig. S18), yielding only a slightly lower barrier (12.8 kcal/mol). However, the hydride transfer
585 to FAD proceeds with a barrier of only 14.1 kcal/mol. This result suggests that the RHR for
586 CHON should proceed with the highest rate of all investigated substrates. Unfortunately, due

587 to the low water solubility of CHON, it was not possible to directly compare the Acmb
588 dehydrogenation rate of CHON and AD¹².

589 It was also observed that 1,2-dehydrogenation can proceed even if a 2 β position is substituted
590 by a hydroxy group⁶⁰. This suggested that 3-ketosteroid can also be activated by an abstraction
591 of the equatorial 2 α H atom by Y363. We decided to test if such activation yields a kinetically
592 accessible energy profile. To abstract the 2 α H atom, Y363 has to break the H-bond with Y118,
593 which in turn forms an H-bond with the 3-keto group (Figure S15). Despite the increased
594 nucleophilic character of the tyrosyl ion, the **TS1** is reached at the later stage and the barrier is
595 higher by 3 kcal/mol compared to the barrier of 2 β H and also higher than the barrier of hydride
596 transfer (Figure S18). This demonstrates that although the enzyme has a preference for the
597 abstraction of the axial 2 β H, the enantioselectivity is not obligatory.

598

599 **Table 2.** Free Energy Barriers (ΔG^\ddagger in kcal/mol) for reactions catalysed by Acmb with 17-MT,
600 DHT and AD and its mutants in reaction with AD as well as experimental relative specific
601 activities (rSA) with respect to reaction conducted with WT enzyme and AD at pH 6.5 with
602 DCPIP.

Acmb variant	Substrate	TS1	I	TS2	P	rSA [%]
WT 2 β H	AD	13.2	2.7	15.5	-9.2	100
WT 2 α H	AD	16.3	2.7	15.5	-9.2	-
WT	17-MT	13.6	2.8	15.6	-9.2	71
WT	DHT	16.5	5.9	19.0	-10.4	19
WT	CHON	12.8	2.8	14.1	-9.5	n.d.*
Y118F	AD	10.8	4.7	21.6	-1.4	Trace
Y115F	AD	12.2	5.2	18.9	-0.9	32
Y467F	AD	14.0	5.3	16.7	-6.1	58

Y536F	AD	9.9	9.4	28.7	2.4	0.6
Y363F	AD	-	-	-	-	0

603 * Activity assay required the addition of cyclodextrin, which makes it incomparable to the
604 assay without one ¹².

605 **Effect of mutations**

606 As expected, the Y363F mutation of AcnB that eliminates the tyrosyl residue from the active
607 site renders the enzyme completely inactive (Tables 3 and S7). The second most severe
608 mutation is Y118F, which interrupts the H-bond with Y363. We were not able to determine the
609 activity of the mutant enzyme in a spectrophotometric assay, but we detected the product after
610 overnight incubation. The QM/MM modelling (Figure S22 and S25) showed that the Y118F
611 mutation facilitates proton removal from the substrate (**TS1** lowered by 2.3 kcal/mol), but the
612 enolate intermediate is less stable and the barrier of the hydride transfer is increased by 6.1
613 kcal/mol. This can be explained by an increased nucleophilic character of the Y363 ion which
614 is not moderated by the H-bond with Y118, as depicted by a much lower charge on the Y363
615 oxygen atom in Y118F vs. WT enzyme (q^{APT} -0.9 vs -0.46, respectively). However, the lack of
616 an additional H-bond with Y118 and enolic intermediate's 3-keto group results in increased
617 energy of **E:I** and **TS2**, due to worse enolate stabilization (i.e. higher charge of O atom bound
618 to C3 and at C2 atom in Y118F than in the WT).

619 Mutation of the Y536 also has a severe impact on enzyme activity (0.6% of the WT). In our
620 modelling, G540 took over the role of Y536 in the stabilization of substrate binding, forming
621 an H-bond with a 3-keto group ($d(\text{C3=O} \cdots \text{HN-G540})$ is 2.1 Å, Figure S24). The position of the
622 substrate was very similar to the WT and the proton abstraction turned out to be very easy (**TS1**
623 of 9.85 kcal/mol, Figure S25). However, upon deprotonation, the conformation of the ring A in
624 the substrate changed, shifting the C3=O group away from G540 and breaking the H-bond. As
625 a result, only two tyrosine residues are involved in the interaction with enolate resulting in a

626 small stabilization of the intermediate (by 0.35 kcal/mol) and difficult hydride transfer (**TS2** 35
627 kcal/mol).

628 Furthermore, we have assessed mutations of the tyrosines involved in the proton relay using
629 Y115F and Y467F mutants (Figures S21 and S23). These variants exhibited decreased specific
630 activities of 32 and 58% with respect to the WT enzyme. These mutations practically did not
631 change the height of the **TS1** barrier (differences within 1 kcal/mol) but lowered the
632 stabilization of **E:I** by 2.6 kcal/mol and slightly increased the energy of **TS2** (1.1 – 3.4
633 kcal/mol). This effect may be associated with the decreased polarity of the active site upon
634 substitution of the tyrosine residue by phenylalanine and with partial disruption of the proton
635 relay system, which utilizes both Y115 and Y467 (Figure S14).

636 Finally, we studied the mutation G540P, which aimed at removing the auxiliary H-bond
637 between the main chain amino group and the 3-keto group of the substrate. However, structural
638 interference introduced by the proline resulted in misfolding of the enzyme. Despite that, we
639 were still able to detect trace activity after overnight incubation of the enzyme with the
640 substrate. Unfortunately, we had to assume that the introduced mutation resulted in a severe
641 change in the protein structure, which does not allow for the modelling of this effect nor gives
642 any insight into the structure of the **E:S** complex.

643

644 **Kinetic Isotope Effect**

645 To gain better insight into the reaction mechanism catalysed by AcnB, we decided to
646 determine the kinetic isotope effect at pH 6.5 and 8.5 (Table 3). We applied two methods: i) a
647 direct method that compared enzyme activities with the unlabelled or labelled substrates
648 measured independently under steady-state and substrate saturation conditions and ii) a
649 competitive method where the equimolar mixture of the unlabelled and labelled substrate was
650 converted by the enzyme while we analysed the composition of the product with LC-MS

651 (Figure S25). The former method yields a ratio of k_{cat} in steady-state which is dependent on
 652 both substrate oxidation and enzyme reoxidation, while the latter method also takes into account
 653 the differences in K_m of the substrate isotopologues yielding $D \left(\frac{V}{K} \right)$. We observed a very small
 654 KIE at pH 6.5 regardless of the substitution position (1.05 and 1.17 respectively for substrate
 655 deuterated at C1 and C2, Fig. S26). At pH 8.5, the observed KIE for C1 substituted substrate
 656 turned out to be slightly higher (1.33) compared to the C2 substituted substrate (1.06). The
 657 competitive experiments yielded $^D(V/K)$ values slightly higher but still in the range of only 1.2–
 658 1.5.

659
 660

661 Table 3. Results of the experimental kinetic isotope effect obtained for C1-substituted DHT
 662 and C2-substituted 17-MT.

Method	Direct method		Competitive method	
Deuterated atom	C1 1,16,16,17-d ₄ - DHT	C2 2,2,4,6,6-d ₅ -17- MT	C1 1,16,16,17-d ₄ - DHT	C2 2,2,4,6,6-d ₅ -17- MT
pH 6.5	1.05 ± 0.04	1.17 ± 0.02	1.50 ± 0.02	1.21 ± 0.01
pH 8.5	1.33 ± 0.08	1.06 ± 0.03	1.23 ± 0.02	1.28 ± 0.01

663
 664 The experimental results on KIE were confronted with the modelling and theoretical prediction
 665 of intrinsic KIE associated with particular molecular steps, as well as the overall KIE associated
 666 with the RHR process estimated with the use of free energy barriers and the Eyring equation⁶¹
 667 (Tables S8-S10).

668 In the case of 2,2,4,6,6-d₅-17-MT, we predicted a high KIE (Tables S8-S10) associated with
 669 the deprotonation of the C2 atom (**S**→**TS1**, 5.3±0.19) and a transition from the intermediate
 670 back to the substrate (**I**→**TS1**, 3.55±0.20), as well as an inverse KIE resulting from hydride
 671 transfer (**I**→**TS2**, 0.7±0.03).

672 For C1 substituted 1,16,16,17-d₄-DHT, calculations suggest a high value of KIE for the
673 hydride transfer (**I**→**TS2**, 4.23±0.03) and a much lower one (close to unity) for the other effects
674 associated with the deprotonation at C2. The overall KIE for the whole RHR estimated with 1
675 kcal/mol accuracy turned out to be in the range of 1.07–2.14 for C2 substituted 17-MT and
676 4.42–4.96 for C1 substituted DHT. These results indicate that the experimentally observed
677 kinetics is limited by some other process not associated with RHR, as KIE although still
678 noticeable, is severely decreased.

679

680 DISCUSSION

681 The analysis of Acmb crystal structure reveals that its structure is similar to that reported
682 previously for KstD1 from *R. erythropolis*, with the exception of a 40-amino acid long
683 membrane-associated domain that is localized in close vicinity of the active site previously
684 referred to as the 'loop'. Helix 8 and 9 of this domain exhibit amphipathic character enabling its
685 anchoring to the membrane. Theoretical prediction indicates that such anchoring positions the
686 enzyme active site oriented toward the membrane surface, which may facilitate the formation
687 of the enzyme-substrate complex even with highly hydrophobic steroids. This domain also
688 narrows the entrance to the active site and strongly interacts with the extended alkyl sidechain
689 in cholest-4-en-3-one, a native substrate of Acmb¹². Prediction of $\Delta G_{\text{binding}}$ and the energy of
690 interaction supports this hypothesis, especially compared to the results calculated for KstD1,
691 which lacks preference for binding cholest-4-en-3-one over steroids with degraded C17
692 substituent. The presence of a loop within the active centre of KstD1 that may affect the
693 enzyme-catalysed reactions was previously reported for several homologous models by Luo *et*
694 *al*¹⁰. The long loops (which could also form elements of secondary structure) may also
695 negatively affect the enzyme activity by hindering substrate access to the active site⁵⁸.

696 The secondary structure of the putative membrane-associated domain, a combination of β -
697 sheets and α -helices, turned out to be much more complex than previously predicted by
698 homology modelling^{10,26}. The bioinformatic analysis of KstD sequences with known biological
699 functions shows the prevalent presence of this domain in the enzyme class. Furthermore, the
700 sequences differ significantly, forming separate clades. Although the data on the substrate
701 specificity of the representatives of each clade is still not plentiful, we suspect that the
702 differences in the sequence of the membrane-associated domain are partially responsible for the
703 reported differences in the substrate specificity. Enzymes belonging to the ReKstD1-like clade
704 all lack a membrane-associated domain and are reported to be inactive or slightly active with
705 C17-substituted steroids^{10,12}. We already demonstrated that ReKstD1 converts cholest-4-en-3-
706 on if proper solubilization is provided. Still, ReKstD1 has a definitively higher preference for
707 smaller substrates. Until now, the only characterized members of Acmb and AmcB2-like clads
708 are Acmb and Acmb2, which are both capable of converting C17-substituted substrates,
709 although with different structural characteristics¹². Moreover, KstD3 from *P. simplex*, a
710 representative of the PsKstD3-like clade, has been reported as active with cholest-4-en-3-one
711 along with several other isoenzymes for which this activity was not observed. Interestingly, a
712 similar phylogenetic tree can be obtained when only sequences of the membrane-associated
713 domain are taken into consideration (Figure S3). As a result, we shall assume that the sequence
714 of the putative membrane-associated domain strongly influences the divergence of the KstD
715 family and may be responsible for the different biological roles of particular enzymes.
716 However, this issue needs further research and a reanalysis of enzyme activities for cholest-4-
717 en-3-on with the use of a cyclodextrin solubilizer.

718 As expected, the substrate specificity is not solely controlled by the putative membrane-
719 associated domain but by the structure of the active site. We have observed differences in ΔG
720 binding even between steroid substrates with relatively similar structures. The sequence

721 alignment analysis of 82 KstDs, as well as the previous report⁶, revealed that many of the
722 residues in the 5 Å radius of the steroid ligand are highly conserved among all clads of the
723 KstDs. The anchoring motive of the 3-ketosteroid group (⁵³⁶YhGhG⁵⁴⁰) is highly conserved as
724 well as catalytically critical Y363 and Y118. The rest of the tyrosine residues forming the proton
725 relay systems are less conserved, with Y115, Y466 and Y467 present in 75, 68 and 69% of the
726 analysed sequences, respectively. Interestingly, the substitution of Y466 and Y467
727 (predominantly by F) strongly correlates with the lack of the membrane-associated domain. The
728 hydrophobic residues that interact with the substrate (A52, F338, A539) are usually substituted
729 by other residues with similar biochemical properties (G52, L338, and P538 in 86%, 55% and
730 52% sequences, respectively). Our modelling confirmed the structure-based hypothesis that
731 both Y536 and the main chain of G540 are involved in the directional binding of 3-ketosteroids.
732 However, the structure of **E:S** appears to be far less rigid than could be expected for such a
733 bulky substrate and sometimes, the substrates are bound less tightly by only one of these
734 residues. This is especially true for DHT, which, due to the different conformation of the ring
735 A from Δ^4 -steroids, does not form a very strong H-bond interaction with Y536 like AD or
736 CHON. The slightly less effective stabilization of enolate is additionally compounded by the
737 lack of a double bond conjugated with the C3 keto group that results in higher charge separation
738 observed in **E:I** when compared to Δ^4 -unsaturated substrates. These two factors seem to be
739 responsible for the overall increase of ΔG for both barriers and the intermediate product (**E:I**).
740 Although we were only able to verify these calculations with steady-state kinetics, which
741 revealed a 5-fold slower oxidation of DHT with respect to AD, we can assume that in the case
742 of DHT, it is the RHR which predominantly controls the observed enzyme activity instead of
743 OHR, as is the case with the other substrates which are oxidized faster. Therefore, we propose
744 that this may explain the observed differences in KstD specificity toward solely Δ^4 -3-
745 ketosteroid⁶. The modelling also confirmed our previous kinetic analysis which pointed out at

746 cholest-4-en-3-one as a native substrate¹². Not only is CHON preferentially bound by the
747 enzyme (the lowest total and the best ΔG and IE), but also its RHR is associated with the lowest
748 barriers for both C-H activation and H⁻ transfer.

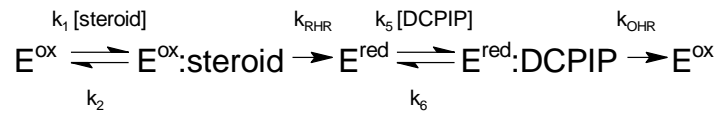
749 Our combined kinetic and modelling studies confirmed that, despite its peculiarities and
750 seemingly different pH of operation from the majority of KstDs, AcmB catalyzes Δ^1 -
751 dehydrogenation according to the Ping-Pong bi-bi kinetics while the RHR proceeds according
752 to the classical two-step mechanisms. The QM/MM MD modelling confirmed an E1cB
753 mechanism for RHR. We have shown that the reaction can proceed under simulated slightly
754 acidic pH of 6.5, provided Y363 is in a deprotonated state, and the obtained free energy surfaces
755 (FESs) are very similar to those reported previously for the dehydrogenation of 17-MT and
756 DHT by KstD1 from *R. erythropolis*. We have demonstrated that the stereoselectivity of
757 activation at the C2 atom is mostly kinetic with the abstraction of 2 β H atom approximately 6.5-
758 fold faster than 2 α H, which is in qualitative agreement with the 10% yield of 2 β -hydroxy-
759 androstenedione reported by Hayano *et al* over 60 years ago⁶⁰. We have further supported this
760 conclusion by showing how deuteration at the 2 β position can decrease the enantioselectivity
761 of C-H activation in 1,2-hydrogenation catalysed by AcmB in D₂O⁶².

762 There are two essential questions arising from our experiment with isotope-labelled
763 substrates. The first question is, why does isotopic substitution at any of the C1 or C2 positions
764 result in a measurable KIE? Second, if RHR is the only isotope-sensitive part of the reaction to
765 such substitution and if OHR is indeed much slower than RHR (as our preliminary pre-steady
766 state kinetics suggests) should KIE be observable at all under the steady-state conditions?

767 The answer to the first question is related to the shape of the free energy profile obtained for
768 AcmB. By considering it within the precision of computational methods (*c.a.* 1 kcal/mol), we
769 found that both substitutions, at 2 β and 1 α positions, significantly reduced the reaction rate of
770 the RHR. The free energy barriers are so close to each other that both of them have a significant

771 impact on the RHR reaction rate. A detailed explanation of a similar situation can be found in
 772 our previous paper related to KstD1 from *R. erythropolis*²⁷.

773 Investigation of the second question requires an analysis of the kinetic equations for the Ping-
 774 Pong bi-bi mechanism. In our case (only RHR sensitive for isotopic substitution) expressions
 775 for steady-state k_{cat} and $KIE(k_{cat})$ are as follows⁶³:



776

$$777 \quad k_{cat \text{ steady-state}} = \frac{k_{RHR} \cdot k_{OHR}}{k_{RHR} + k_{OHR}}$$

$$778 \quad KIE_{\text{steady-state}} = \frac{KIE_{RHR} + \frac{k_{RHR}}{k_{OHR}}}{1 + \frac{k_{RHR}}{k_{OHR}}}$$

779

780 As we were not able to obtain an experimental value of KIE for RHR due to the too high rate
 781 of the process, it was not possible to determine the experimental ratio of k_{RHR}/k_{OHR} . Still, we
 782 could use our computational estimations, so in Table 4, we presented calculated values of
 783 $KIE_{\text{steady-state}}$ in a function of potential KIE_{RHR} (in the range of 1.07-4.96) and the ratio between
 784 k_{RHR} to k_{OHR} .

785

786
787

Table 4. Calculated values of $KIE_{\text{steady-state}}$ in the function of KIE_{RHR} and $k_{\text{RHR}}/k_{\text{OHR}}$

KIE_{RHR}	$k_{\text{RHR}}/k_{\text{OHR}}$				
	1	10	25	50	100
1.07	1.04	1.01	1.00	1.00	1.00
1.50	1.25	1.05	1.02	1.01	1.01
2.00	1.50	1.09	1.04	1.02	1.01
3.00	2.00	1.18	1.08	1.04	1.02
4.00	2.50	1.27	1.12	1.06	1.03
4.96	2.98	1.36	1.15	1.08	1.04

788

789 Although our analysis is approximate, it demonstrates that it is possible to observe KIE in the
790 steady-state experiment, even when the process related to OHR is a hundred times slower than
791 the RHR. Based on our preliminary pre-steady-state kinetics, we expect that at an optimal pH
792 of 6.5 OHR should be at least 10 times slower than RHR, which would explain the experimental
793 KIE in the range of 1.05–1.33. We have seen a similar masking effect in our recent study of
794 KstD1, but k_{OHR} and k_{RHR} were estimated as of the same magnitude²⁷. As a result, we observed
795 higher values of the steady-state KIE for KstD1 (1.28 for 17-MT and 1.5 for DHT) than for
796 Acmb (1.06–1.17 for 17-MT and 1.05–1.33 for DHT).

797 We were also able to investigate the effects of Y to F mutations in the active site of Acmb
798 on the free energy profile of RHR. Our mutations introduced a minimal disturbance to the
799 protein structure, only removing the tyrosyl OH group. These mutations can be divided into
800 two groups, those targeting the proton relay system (Y115F and Y467F) and those directly
801 interfering with the substrates' activation and enolate stabilization (Y536F, Y363F, Y118F).
802 Our bioinformatic analysis showed (KstDs from ReKstD1-like clade) that tyrosines of the

803 proton relay system are not obligatory for KstD activity. Their substitution to phenylalanine
804 results in a moderate decrease (2-3 fold) in the specific activity and slightly increases the barrier
805 (TS2) of the hydride transfer to FAD. On the other hand, any mutation of tyrosines involved in
806 catalysis leaves KstD either unable to activate the substrate (Y363F) or, while making the
807 abstraction of the 2Hb proton easier, prohibitively increases the barrier of hydride transfer,
808 rendering KstD virtually inactive.

809 Finally, we have shown, that RHR proceeds at a constant rate in a wide pH range (7.5–10)
810 with a slight optimum at pH 9.0. Based on our preliminary pre-steady state it seems that OHR
811 with DCPIP is slower than RHR and as a result, is controlling the steady-state kinetics and
812 determining a steady-state pH optimum at 6.5. Unfortunately, unlike KstD1 from *R.*
813 *erythropolis*, Acmb turned out to be a poor subject for pre-steady state kinetics. Its RHR at
814 substrate-saturated conditions proceeds too fast for the stopped-flow equipment while the
815 concentrated, reduced enzyme exhibited fast aggregation below pH 7.5, preventing
816 investigation of OHR kinetics at 6.5.

817 **Conclusions**

818 We determined the structure of KstD from *S. denitrificans* (Acmb) demonstrating for the first
819 time the structure of the so-called 'loop' which is a characteristic motif for the majority of the
820 known KstD sequences. This putative membrane-associated domain may be responsible for
821 anchoring the enzyme to the cytoplasmic membrane, positioning the enzyme active site toward
822 the source of the substrate as well as stabilization of the E:S complex with C17-substituted 3-
823 ketosteroids. With QM/MM MD modelling and kinetic studies, we confirmed that the 1,2-
824 dehydrogenation catalysed by Acmb proceeds according to the Ping-Pong bi-bi mechanism,
825 while RHR according to the accepted two-step elimination mechanism. We showed that OHR,
826 not RHR, is responsible for the low values of KIE observed in the steady-state experiments as
827 well as peculiar pH optima. As in the case of KstD1 from *R. erythropolis*, the nature of FES is

828 responsible for the KIE observed for both C1 and C2 labelled substrates, which once again
829 demonstrates that our findings are general for KstD class. Our modelling also provided
830 quantitative insight into the role of active site tyrosines, the influence of the Δ^4 -double bond in
831 the steroid on its activity and corroborated experimental evidence on non-obligatory
832 enantioselectivity during C-H activation.

833 **Data availability**

834 Atomic coordinates and structure factors corresponding to the final crystallographic models
835 of Acmb generated in this study have been deposited in the Protein Data Bank (PDB) under
836 the accession code 7P18. The corresponding raw diffraction images have been deposited in the
837 Integrated Resource for Reproducibility in Macromolecular Crystallography
838 (<https://proteindiffraction.org/>) under DOI: 10.18430/M37P18. The computational data are
839 available on request.

840 ASSOCIATED CONTENT

841 AUTHOR INFORMATION

842 **Corresponding Author**

843 Maciej Szaleniec – Jerzy Haber Institute of Catalysis and Surface Chemistry, Polish Academy
844 of Sciences, 30-239 Krakow, Poland; orcid.org/0000-0002-7650-9263; Email:
845 maciej.szaleniec@ikifp.edu.pl

846 **Author Contributions**

847 P.W. purified and crystalized the enzyme, determined and refined the enzyme structure,
848 developed LC-MS methods, conducted kinetics (pH, mutated variants, kinetic isotope effect),
849 analysed results, co-authored and edited manuscript, and created figures
850 M.G. conducted all calculations, analysed results, developed discussion, co-authored the main
851 text, edited text, and created figures
852 B.M. refined the structure of Acmb, co-authored the manuscript
853 M.P. conducted stopped-flow steady-state and pre-steady state kinetics, co-authored method
854 section

855 O.Z. developed Acmb mutant variants, expressed and purified the enzymes,
856 M.F. conducted stopped-flow steady-state Ping Pong kinetics, analysed results
857 K.K. refined the structure of Acmb, co-authored the manuscript (crystallographic sections)
858 M.O. provided assistance in pre-steady state kinetics, edited the manuscript
859 A.B. supervised P.W., provided funding, edited the manuscript
860 E.N. developed conditions for enzyme crystallization, edited the manuscript
861 W.M. oversaw initial experiments and edited the manuscript
862 A.M.W. purified the enzyme, conducted the bioinformatic analysis, co-authored the
863 bioinformatic analysis section, created figures
864 M.S. designed the study, provided funding, supervised M.G, P.W., M.P., O.Z., M. F.,
865 analysed and curated all data, co-authored and edited the manuscript,
866

867 The manuscript was written with the contributions of all authors. All authors have approved
868 the final version of the manuscript.

869 **Funding Sources**

870 The National Science Centre Poland under the OPUS grant number UMO-
871 2016/21/B/ST4/03798.

872 The National Centre of Research and Development POWR. 03.02.00-00-I013/16.

873 **Notes**

874 The authors declare that they have no competing financial interests.

875 **ACKNOWLEDGMENT**

876 The authors acknowledge financial support from the National Science Centre Poland under
877 the OPUS grant number UMO-2016/21/B/ST4/03798. M.G and P.W. acknowledge the
878 fellowship under InterDokMed project no. POWR. 03.02.00-00-I013/16. The computational
879 time was supported by PL-Grid Infrastructure (CYFRONET). The QMMM MD calculations
880 were conducted with fDynamo programs developed by BioComp group from Universitat Jaume
881 I, Castellón, Spain. We acknowledge the joint consortium “Interdisciplinary Centre of Physical,
882 Chemical and Biological Sciences” of ICSC PAS and INP PAS for providing access to the

883 Agilent 1290 Infinity System with an automatic autosampler and an MS Agilent 6460 Triple
884 Quad Detector. XRD measurements were carried out at the 14.1 beamline at the BESSY II
885 electron storage ring operated by the Helmholtz-Zentrum Berlin für Materialien und Energie.
886 We would like to thank Piotr Wilk (Małopolska Centre of Biotechnology, Jagiellonian
887 University) for his assistance during the experiment.

888 ABBREVIATIONS

889 Acmb (Anaerobic cholesterol metabolism enzyme B), KstD (3-ketosteroid dehydrogenase),
890 AD (androst-4-en-3-one), DHT – dihydrotestosterone, 17-MT – 17-methyltestosterone, PRG
891 – progesterone, 6-DHA – 6-dehydrotestosterone acetate, TP – testosterone propionate, DGN –
892 diosgenone, CHON – cholest-4-en-3-one

893 Supporting Information

894 The Supporting Information is available free of charge at ...

895 Extended experimental procedure (Site-directed mutagenesis, Kinetic isotope effect–
896 competition method, QMMM model setup), phylogenetic tree for ‘loop’ sequences of KstDs
897 and six-tyrosine motif analysis, sequence alignment of 82 KstDs, diffraction data collection
898 and refinement statistics, Size-exclusion chromatograms of Acmb, figures and mobility
899 analyses of putative membrane-associated domain, figures of Acmb structure, binding sites,
900 details on MMPBSA $\Delta G_{\text{binding}}$ and interaction energies for Acmb and KstD1, details on MD
901 trajectories, figures of stationary states of all mechanisms and figures depicting PES profiles,
902 detailed data on activities of mutants, experimental and theoretical kinetic isotope effects,
903 PDB files of representative structures optimized at the B3LYP/AMBER level of theory

904

905

906 REFERENCES

- 907 (1) Hosta-Rigau, L.; Zhang, Y.; Teo, B. M.; Postma, A.; Städler, B. Cholesterol - A
908 Biological Compound as a Building Block in Bionanotechnology. *Nanoscale* **2013**, *5*
909 (1), 89–109. <https://doi.org/10.1039/c2nr32923a>.
- 910 (2) Costa, S.; Zappaterra, F.; Summa, D.; Semeraro, B.; Fantin, G. By Rhodococcus Strains.
911 **2020**, 1–12.
- 912 (3) Tong, W.; Dong, X. Microbial Biotransformation: Recent Developments on Steroid
913 Drugs. *Recent Pat. Biotechnol.* **2009**, *3* (2), 141–153.
914 <https://doi.org/10.2174/187220809788700157>.
- 915 (4) Omar, M; Khan, F; Lee, H. j. *Synthesis and Pharmacology of Anti-Inflammatory*
916 *Steroid Antedrugs*; 2008; Vol. 108. <https://doi.org/10.1021/cr068203e>.Synthesis.
- 917 (5) Zhang, H.; Tian, Y.; Wang, J.; Li, Y.; Wang, H.; Mao, S.; Liu, X. Construction of
918 Engineered Arthrobacter Simplex with Improved Performance for Cortisone Acetate
919 Biotransformation. *Appl. Microbiol. Biotechnol.* **2013**, *97* (21), 9503–9514.
920 <https://doi.org/10.1007/s00253-013-5172-7>.
- 921 (6) Rohman, A.; Dijkstra, B. W. The Role and Mechanism of Microbial 3-Ketosteroid Δ 1-
922 Dehydrogenases in Steroid Breakdown. *J. Steroid Biochem. Mol. Biol.* **2019**, *191*,
923 105366. <https://doi.org/10.1016/j.jsbmb.2019.04.015>.
- 924 (7) Donova, M. V; Egorova, O. V. Microbial Steroid Transformations: Current State and
925 Prospects. *Appl. Microbiol. Biotechnol.* **2012**, *94* (6), 1423–1447.
926 <https://doi.org/10.1007/s00253-012-4078-0>.
- 927 (8) Rohman, A.; Dijkstra, B. W. Application of Microbial 3-Ketosteroid Δ 1-

- 928 Dehydrogenases in Biotechnology. *Biotechnol. Adv.* **2021**, *49*, 107751.
929 <https://doi.org/10.1016/j.biotechadv.2021.107751>.
- 930 (9) Chiang, Y. R.; Ismail, W.; Gallien, S.; Heintz, D.; Van Dorsselaer, A.; Fuchs, G. Cholest-
931 4-En-3-One- Δ 1-Dehydrogenase, a Flavoprotein Catalyzing the Second Step in Anoxic
932 Cholesterol Metabolism. *Appl. Environ. Microbiol.* **2008**, *74*, 107–113.
933 <https://doi.org/10.1128/AEM.01968-07>.
- 934 (10) Luo, J. M.; Cui, H. L.; Jia, H. C.; Li, F.; Cheng, H. J.; Shen, Y. B.; Wang, M.
935 Identification, Biological Characteristics, and Active Site Residues of 3-Ketosteroid Δ 1-
936 Dehydrogenase Homologues from *Arthrobacter Simplex*. *J. Agric. Food Chem.* **2020**, *68*
937 (35), 9496–9512. <https://doi.org/10.1021/acs.jafc.0c03360>.
- 938 (11) Wojtkiewicz, A. M.; Wójcik, P.; Procner, M.; Flejszar, M.; Oszejca, M.; Hochołowski,
939 M.; Tataruch, M.; Mrugała, B.; Janeczko, T.; Szaleniec, M. The Efficient Δ 1-
940 Dehydrogenation of a Wide Spectrum of 3-Ketosteroids in a Broad PH Range by 3-
941 Ketosteroid Dehydrogenase from *Sterolibacterium Denitrificans*. *J. Steroid Biochem.*
942 *Mol. Biol.* **2020**, *202* (April), 105731. <https://doi.org/10.1016/j.jsbmb.2020.105731>.
- 943 (12) Wójcik, P.; Glanowski, M.; Wojtkiewicz, A. M.; Rohman, A.; Szaleniec, M. Universal
944 Capability of 3-ketosteroid Δ 1 Dehydrogenases to Catalyze Δ 1-dehydrogenation of C17
945 -substituted Steroids. *Microb. Cell Fact.* **2021**, *20* (119), 1–12.
946 <https://doi.org/10.1186/s12934-021-01611-5>.
- 947 (13) Rohman, A.; Van Oosterwijk, N.; Thunnissen, A. M. W. H.; Dijkstra, B. W. Crystal
948 Structure and Site-Directed Mutagenesis of 3-Ketosteroid Δ 1-Dehydrogenase from
949 *Rhodococcus Erythropolis* SQ1 Explain Its Catalytic Mechanism. *J. Biol. Chem.* **2013**,
950 *288* (49), 35559–35568. <https://doi.org/10.1074/jbc.M113.522771>.

- 951 (14) Oxford Diffraction, 2006. CrysAlis Pro Oxford Diffraction Ltd, Version 1.171.36.20
952 (Release 27-06-2012 CrysAlis171.NET), Abingdon, England.
- 953 (15) Kabsch, W. XDS. *Acta Crystallogr. Sect. D* **2010**, *66*, 125–132.
954 <https://doi.org/10.1107/S0907444909047337>.
- 955 (16) Adams, P. D.; Pavel, V.; Chen, V. B.; Ian, W.; Echols, N.; Moriarty, N. W.; Read, R. J.;
956 Richardson, D. C.; Jane, S.; Thomas, C. PHENIX: A Comprehensive Python-Based
957 System for Macromolecular Structure Solution. *Acta Crystallogr. Sect. D Biol.*
958 *Crystallogr.* **2010**, *66*, 213–221. <https://doi.org/10.1107/S0907444909052925>.
- 959 (17) Winn, M. D.; Ballard, C. C.; Cowtan, K. D.; Dodson, E. J.; Emsley, P.; Evans, P. R.;
960 Keegan, R. M.; Krissinel, E. B.; Leslie, A. G. W.; McCoy, A. J.; S.McNicholas;
961 Murshudov, G. N.; Pannu, N. S.; Potterton, E. A.; Powell, H. R.; Read, R. J.; Vagin, A.;
962 Wilson, K. S. Overview of the CCP4 Suite and Current Developments. *Acta Crystallogr.*
963 *Sect. D Biol. Crystallogr.* **2011**, *67*, 235–242.
964 <https://doi.org/10.1107/S0907444910045749>.
- 965 (18) Murshudov, G. N.; Skubák, P.; Lebedev, A. A.; Pannu, N. S.; Steiner, R. A.; Nicholls,
966 R. A.; Winn, M. D.; Longa, F.; Vagina, A. A. REFMAC 5 for the Refinement of
967 Macromolecular Crystal Structures. *Acta Crystallogr. Sect. D Biol. Crystallogr.* **2011**,
968 *67*, 355–367. <https://doi.org/10.1107/S0907444911001314>.
- 969 (19) Emsley, P.; Lohkamp, B.; Scott, W. G.; Cowtan, K. Features and Development of Coot.
970 *Acta Crystallogr. Sect. D Biol. Crystallogr.* **2010**, *66*, 486–501.
971 <https://doi.org/10.1107/S0907444910007493>.
- 972 (20) Chen, V. B.; Arendall III, W. B.; Headd, J. J.; Keedy, D. A.; Immormino, R. M.; Kapral,
973 G. J.; Murray, L. W.; Richardson, J. S.; Richardson, D. C. MolProbity: All-Atom

- 974 Structure Validation for Macromolecular Crystallography. *Acta Crystallogr. Sect. D*
975 *Biol. Crystallogr.* **2009**, *66*, 12–21. <https://doi.org/10.1107/S09074444909042073>.
- 976 (21) Young, J. Y.; Westbrook, J. D.; Feng, Z.; Sala, R.; Peisach, E.; Oldfield, T. J.; Sen, S.;
977 Gutmanas, A.; Armstrong, D. R.; Berrisford, J. M.; Chen, L.; Chen, M.; Di Costanzo, L.;
978 Dimitropoulos, D.; Gao, G.; Ghosh, S.; Gore, S.; Guranovic, V.; Hendrickx, P. M. S.;
979 Hudson, B. P.; Igarashi, R.; Ikegawa, Y.; Kobayashi, N.; Lawson, C. L.; Liang, Y.;
980 Mading, S.; Mak, L.; Mir, M. S.; Mukhopadhyay, A.; Patwardhan, A.; Persikova, I.;
981 Rinaldi, L.; Sanz-Garcia, E.; Sekharan, M. R.; Shao, C.; Swaminathan, G. J.; Tan, L.;
982 Ulrich, E. L.; van Ginkel, G.; Yamashita, R.; Yang, H.; Zhuravleva, M. A.; Quesada, M.;
983 Kleywegt, G. J.; Berman, H. M.; Markley, J. L.; Nakamura, H.; Velankar, S.; Burley, S.
984 K. OneDep: Unified WwPDB System for Deposition , Biocuration , and Validation of
985 Macromolecular Structures in the PDB Archive. *Structure* **2017**, *25* (3), 536–545.
986 <https://doi.org/10.1016/j.str.2017.01.004>.
- 987 (22) The PyMOL Molecular Graphics System, Version 1.2r3pre, Schrödinger, LLC.
- 988 (23) Pettersen, E. F.; Goddard, T. D.; Huang, C. C.; Couch, G. S.; Greenblatt, D. M.; Meng,
989 E. C.; Ferrin, T. E. UCSF Chimera — A Visualization System for Exploratory Research
990 and Analysis. *J. Comput. Chem.* **2004**, *25* (13), 1605–1612.
991 <https://doi.org/10.1002/jcc.20084>.
- 992 (24) BIOVIA, Dassault Systèmes, Discovery Studio, V21.1.0.20298, San Diego: Dassault
993 Systèmes, 2021.
- 994 (25) Lomize, M. A.; Pogozheva, I. D.; Joo, H.; Mosberg, H. I.; Lomize, A. L. OPM Database
995 and PPM Web Server: Resources for Positioning of Proteins in Membranes. *Nucleic*
996 *Acids Res.* **2012**, *40*, 370–376. <https://doi.org/10.1093/nar/gkr703>.

- 997 (26) Sofińska, K.; Wojtkiewicz, A. M.; Wójcik, P.; Zastawny, O.; Guzik, M.; Winiarska, A.;
998 Waligórski, P.; Cieśla, M.; Barbasz, J.; Szaleniec, M. Investigation of Quaternary
999 Structure of Aggregating 3-Ketosteroid Dehydrogenase from Sterolibacterium
1000 Denitrificans: In the Pursuit of Consensus of Various Biophysical Techniques. *Biochim.*
1001 *Biophys. Acta - Gen. Subj.* **2019**, *1863* (6), 1027–1039.
1002 <https://doi.org/10.1016/j.bbagen.2019.03.009>.
- 1003 (27) Glanowski, M.; Wójcik, P.; Procner, M.; Borowski, T.; Lupa, D.; Mielczarek, P.;
1004 Oszejca, M.; Świderek, K.; Moliner, V.; Bojarski, A. J.; Szaleniec, M. Enzymatic Δ 1-
1005 Dehydrogenation of 3-Ketosteroids—Reconciliation of Kinetic Isotope Effects with the
1006 Reaction Mechanism. *ACS Catal.* **2021**, *11* (13), 8211–8225.
1007 <https://doi.org/10.1021/acscatal.1c01479>.
- 1008 (28) Rugor, A.; Wójcik-Augustyn, A.; Niedzialkowska, E.; Mordalski, S.; Staroń, J.;
1009 Bojarski, A.; Szaleniec, M. Reaction Mechanism of Sterol Hydroxylation by Steroid C25
1010 Dehydrogenase – Homology Model, Reactivity and Isoenzymatic Diversity. *J. Inorg.*
1011 *Biochem.* **2017**, *173*. <https://doi.org/10.1016/j.jinorgbio.2017.04.027>.
- 1012 (29) Melander, L. Isotope Effect on Reaction Rates. *Ronald Press Co. New York* **1960**, 46–
1013 64.
- 1014 (30) Madeira, F.; Park, Y. M.; Lee, J.; Buso, N.; Gur, T.; Madhusoodanan, N.; Basutkar, P.;
1015 Tivey, A. R. N.; Potter, S. C.; Finn, R. D.; Lopez, R. The EMBL-EBI Search and
1016 Sequence Analysis Tools APIs in 2019. *Nucleic Acids Res.* **2019**, *47* (W1), W636–W641.
1017 <https://doi.org/10.1093/nar/gkz268>.
- 1018 (31) Waterhouse, A. M.; Procter, J. B.; Martin, D. M. A.; Clamp, M.; Barton, G. J. Jalview
1019 Version 2—a Multiple Sequence Alignment Editor and Analysis Workbench.
1020 *Bioinformatics* **2009**, *25* (9), 1189–1191. <https://doi.org/10.1093/bioinformatics/btp033>.

- 1021 (32) Kabsch, W. A Discussion of the Solution for the Best Rotation to Relate Two Sets of
1022 Vectors. *Acta Crystallogr. Sect. A* **1978**, *34* (5), 827–828.
1023 <https://doi.org/10.1074/jbc.M113.522771>.
- 1024 (33) Søndergaard, C. R.; Olsson, M. H. M.; Rostkowski, M.; Jensen, J. H. Improved
1025 Treatment of Ligands and Coupling Effects in Empirical Calculation and Rationalization
1026 of PKa Values. *J. Chem. Theory Comput.* **2011**, *7* (7), 2284–2295.
1027 <https://doi.org/10.1021/ct200133y>.
- 1028 (34) Olsson, M. H. M.; Søndergaard, C. R.; Rostkowski, M.; Jensen, J. H. PROPKA3:
1029 Consistent Treatment of Internal and Surface Residues in Empirical PKa Predictions. *J.*
1030 *Chem. Theory Comput.* **2011**, *7* (2), 525–537. <https://doi.org/10.1021/ct100578z>.
- 1031 (35) Frisch, M. J.; Trucks, G. W.; Schlegel, H. B.; Scuseria, G. E.; Robb, M. a.; Cheeseman,
1032 J. R.; Scalmani, G.; Barone, V.; Petersson, G. a.; Nakatsuji, H.; Li, X.; Caricato, M.;
1033 Marenich, a. V.; Bloino, J.; Janesko, B. G.; Gomperts, R.; Mennucci, B.; Hratchian, H.
1034 P.; Ortiz, J. V.; Izmaylov, a. F.; Sonnenberg, J. L.; Williams; Ding, F.; Lipparini, F.;
1035 Egidi, F.; Goings, J.; Peng, B.; Petrone, A.; Henderson, T.; Ranasinghe, D.; Zakrzewski,
1036 V. G.; Gao, J.; Rega, N.; Zheng, G.; Liang, W.; Hada, M.; Ehara, M.; Toyota, K.; Fukuda,
1037 R.; Hasegawa, J.; Ishida, M.; Nakajima, T.; Honda, Y.; Kitao, O.; Nakai, H.; Vreven, T.;
1038 Throssell, K.; Montgomery Jr., J. a.; Peralta, J. E.; Ogliaro, F.; Bearpark, M. J.; Heyd, J.
1039 J.; Brothers, E. N.; Kudin, K. N.; Staroverov, V. N.; Keith, T. a.; Kobayashi, R.;
1040 Normand, J.; Raghavachari, K.; Rendell, a. P.; Burant, J. C.; Iyengar, S. S.; Tomasi, J.;
1041 Cossi, M.; Millam, J. M.; Klene, M.; Adamo, C.; Cammi, R.; Ochterski, J. W.; Martin,
1042 R. L.; Morokuma, K.; Farkas, O.; Foresman, J. B.; Fox, D. J. G16_C01. 2016, p Gaussian
1043 16, Revision C.01, Gaussian, Inc., Wallin.
- 1044 (36) Becke, A. D. Density-Functional Thermochemistry. III. The Role of Exact Exchange. *J.*

- 1045 *Chem. Phys.* **1993**, 98 (7), 5648–5652. <https://doi.org/10.1063/1.464913>.
- 1046 (37) Dupradeau, F. Y.; Cézard, C.; Lelong, R.; Stanislawiak, É.; Pêcher, J.; Delepine, J. C.;
1047 Cieplak, P. R.E.D.D.B.: A Database for RESP and ESP Atomic Charges, and Force Field
1048 Libraries. *Nucleic Acids Res.* **2008**, 36 (SUPPL. 1), 360–367.
1049 <https://doi.org/10.1093/nar/gkm887>.
- 1050 (38) Salomon-Ferrer, R.; Case, D. A.; Walker, R. C. An Overview of the Amber Biomolecular
1051 Simulation Package. *Wiley Interdiscip. Rev. Comput. Mol. Sci.* **2013**, 3, 198–210.
1052 <https://doi.org/10.1002/wcms.1121>.
- 1053 (39) Duan, Y.; Wu, C.; Chowdhury, S.; Lee, M. C.; Xiong, G.; Zhang, W.; Yang, R.; Cieplak,
1054 P.; Luo, R.; Lee, T.; Caldwell, J.; Wang, J.; Kollman, P. A Point-Charge Force Field for
1055 Molecular Mechanics Simulations of Proteins Based on Condensed-Phase Quantum
1056 Mechanical Calculations. *J. Comput. Chem.* **2003**, 24 (16), 1999–2012.
1057 <https://doi.org/10.1002/jcc.10349>.
- 1058 (40) Miller, B. R.; Mcgee, T. D.; Swails, J. M.; Homeyer, N.; Gohlke, H.; Roitberg, A. E.
1059 MMPBSA.Py: An Efficient Program for End-State Free Energy Calculations. **2012**.
1060 <https://doi.org/10.1021/ct300418h>.
- 1061 (41) Field, M. J.; Albe, M.; Bret, C.; Proust-De Martin, F.; Thomas, A. The Dynamo Library
1062 for Molecular Simulations Using Hybrid Quantum Mechanical and Molecular
1063 Mechanical Potentials. *J. Comput. Chem.* **2000**, 21 (12), 1088–1100.
1064 [https://doi.org/https://doi.org/10.1002/1096-987X\(200009\)21:12<1088::AID-](https://doi.org/https://doi.org/10.1002/1096-987X(200009)21:12<1088::AID-JCC5>3.0.CO;2-8)
1065 [JCC5>3.0.CO;2-8](https://doi.org/https://doi.org/10.1002/1096-987X(200009)21:12<1088::AID-JCC5>3.0.CO;2-8).
- 1066 (42) Krzemińska, A.; Paneth, P.; Moliner, V.; Świderek, K. Binding Isotope Effects as a Tool
1067 for Distinguishing Hydrophobic and Hydrophilic Binding Sites of HIV-1 RT. *J. Phys.*

- 1068 *Chem. B* **2015**, *119* (3), 917–927. <https://doi.org/10.1021/jp506119h>.
- 1069 (43) Torrie, G. M.; Valleau, J. P. Nonphysical Sampling Distributions in Monte Carlo Free-
1070 Energy Estimation: Umbrella Sampling. *J. Comput. Phys.* **1977**, *23* (2), 187–199.
1071 [https://doi.org/10.1016/0021-9991\(77\)90121-8](https://doi.org/10.1016/0021-9991(77)90121-8).
- 1072 (44) Kumar, S.; Rosenberg, J. M.; Bouzida, D.; Swendsen, R. H.; Kollman, P. A. THE
1073 Weighted Histogram Analysis Method for Free-Energy Calculations on Biomolecules.
1074 I. The Method. *J. Comput. Chem.* **1992**, *13* (8), 1011–1021.
1075 <https://doi.org/10.1002/jcc.540130812>.
- 1076 (45) J. S. Dewar, M.; G. Zoebisch, E.; F. Healy, E.; J. P. Stewart, J. Development and Use of
1077 Quantum Mechanical Molecular Models. 76. AM1: A New General Purpose Quantum
1078 Mechanical Molecular Model. *J. Am. Chem. Soc.* **2002**, *107* (13), 3902–3909.
1079 <https://doi.org/10.1021/ja00299a024>.
- 1080 (46) Ruiz-Pernía, J. J.; Silla, E.; Tuñón, I.; Martí, S.; Moliner, V. Hybrid QM/MM Potentials
1081 of Mean Force with Interpolated Corrections. *J. Phys. Chem. B* **2004**, *108* (24), 8427–
1082 8433. <https://doi.org/10.1021/jp049633g>.
- 1083 (47) Chuang, Y.-Y.; Corchado, J. C.; Truhlar, D. G. Mapped Interpolation Scheme for Single-
1084 Point Energy Corrections in Reaction Rate Calculations and a Critical Evaluation of
1085 Dual-Level Reaction Path Dynamics Methods. *J. Phys. Chem. A* **1999**, *103* (8), 1140–
1086 1149. <https://doi.org/10.1021/jp9842493>.
- 1087 (48) Świderek, K.; Tuñón, I.; Martí, S.; Moliner, V. Protein Conformational Landscapes and
1088 Catalysis. Influence of Active Site Conformations in the Reaction Catalyzed by L-
1089 Lactate Dehydrogenase. *ACS Catal.* **2015**, *5* (2), 1172–1185.
1090 <https://doi.org/10.1021/cs501704f>.

- 1091 (49) Baker, J.; Kessi, A.; Delley, B. The Generation and Use of Delocalized Internal
1092 Coordinates in Geometry Optimization. *J. Chem. Phys.* **1996**, *105* (1), 192–212.
1093 <https://doi.org/10.1063/1.471864>.
- 1094 (50) Martí, S.; Moliner, V.; Tuñón, I. Improving the QM/MM Description of Chemical
1095 Processes: A Dual Level Strategy To Explore the Potential Energy Surface in Very
1096 Large Systems. *J. Chem. Theory Comput.* **2005**, *1* (5), 1008–1016.
1097 <https://doi.org/10.1021/ct0501396>.
- 1098 (51) Ruggiero, G. D.; Guy, S. J.; Martí, S.; Moliner, V.; Williams, I. H. Vibrational Analysis
1099 of the Chorismate Rearrangement: Relaxed Force Constants, Isotope Effects and
1100 Activation Entropies Calculated for Reaction in Vacuum, Water and the Active Site of
1101 Chorismate Mutase. *J. Phys. Org. Chem.* **2004**, *17* (6–7), 592–601.
1102 <https://doi.org/https://doi.org/10.1002/poc.781>.
- 1103 (52) Świderek, K.; Tuñón, I.; Williams, I. H.; Moliner, V. Insights on the Origin of Catalysis
1104 on Glycine N-Methyltransferase from Computational Modeling. *J. Am. Chem. Soc.*
1105 **2018**, *140* (12), 4327–4334. <https://doi.org/10.1021/jacs.7b13655>.
- 1106 (53) Krzemińska, A.; Moliner, V.; Świderek, K. Dynamic and Electrostatic Effects on the
1107 Reaction Catalyzed by HIV-1 Protease. *J. Am. Chem. Soc.* **2016**, *138* (50), 16283–16298.
1108 <https://doi.org/10.1021/jacs.6b06856>.
- 1109 (54) Wang, X.; Feng, J.; Zhang, D.; Wu, Q.; Zhu, D.; Ma, Y. Characterization of New
1110 Recombinant 3-Ketosteroid- Δ 1-Dehydrogenases for the Biotransformation of Steroids.
1111 *Appl. Microbiol. Biotechnol.* **2017**, *101* (15), 6049–6060.
1112 <https://doi.org/10.1007/s00253-017-8378-2>.
- 1113 (55) Guevara, G.; Fernández de las Heras, L.; Perera, J.; Navarro Llorens, J. M. Functional

- 1114 Differentiation of 3-Ketosteroid Δ^1 -Dehydrogenase Isozymes in *Rhodococcus Ruber*
1115 Strain Chol-4. *Microb. Cell Fact.* **2017**, *16* (1), 1–16. [https://doi.org/10.1186/s12934-](https://doi.org/10.1186/s12934-017-0657-1)
1116 [017-0657-1](https://doi.org/10.1186/s12934-017-0657-1).
- 1117 (56) Brzostek, A.; Śliwiński, T.; Rumijowska-Galewicz, A.; Korycka-Machała, M.; Dziadek,
1118 J. Identification and Targeted Disruption of the Gene Encoding the Main 3-Ketosteroid
1119 Dehydrogenase in *Mycobacterium Smegmatis*. *Microbiology* **2005**, *151* (7), 2393–2402.
1120 <https://doi.org/10.1099/mic.0.27953-0>.
- 1121 (57) Van Oosterwijk, N.; Knol, J.; Dijkhuizen, L.; Van Der Geize, R.; Dijkstra, B. W.
1122 Structure and Catalytic Mechanism of 3-Ketosteroid- Δ^4 -(5 α)- Dehydrogenase from
1123 *Rhodococcus Jostii* RHA1 Genome. *J. Biol. Chem.* **2012**, *287* (37), 30975–30983.
1124 <https://doi.org/10.1074/jbc.M112.374306>.
- 1125 (58) Urich, K. Sterols and Steroids BT - Comparative Animal Biochemistry; Urich, K., Ed.;
1126 Springer Berlin Heidelberg: Berlin, Heidelberg, 1994; pp 624–656.
1127 https://doi.org/10.1007/978-3-662-06303-3_16.
- 1128 (59) Dym, O.; Eisenberg, D. Sequence-Structure Analysis of FAD-Containing Proteins.
1129 *Protein Sci.* **2001**, *10* (9), 1712–1728.
- 1130 (60) Hayano, M.; Ringold, H. J.; Stefanovic, V.; Gut, M.; Dorfman, R. I. The Stereochemical
1131 Course of Enzymatic Steroid 1,2-Dehydrogenation. *Biochem. Biophys. Res. Commun.*
1132 **1961**, *4* (6), 454–459. [https://doi.org/http://dx.doi.org/10.1016/0006-291X\(61\)90307-2](https://doi.org/http://dx.doi.org/10.1016/0006-291X(61)90307-2).
- 1133 (61) Eyring, H. The Activated Complex in Chemical Reactions. *J. Chem. Phys.* **1935**, *3* (2),
1134 63–71. <https://doi.org/10.1063/1.1749604>.
- 1135 (62) Wojtkiewicz, A. M.; Glanowski, M.; Waligórski, P.; Janeczko, T.; Szaleniec, M. 1,2-
1136 Hydrogenation and Transhydrogenation Catalyzed by 3-Ketosteroid Δ^1 -

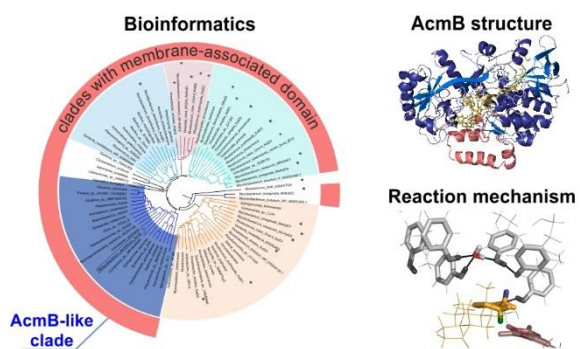
1137 Dehydrogenase from *Sterolibacterium Denitrificans*—Kinetics, Isotope Labelling
1138 and QM:MM Modelling Studies. *International Journal of Molecular Sciences*. 2022.
1139 <https://doi.org/10.3390/ijms232314660>.

1140 (63) Karsten, W. E.; Cook, P. F. Substrate Dependence of Isotope Effects. In *Isotope Effects*
1141 *In Chemistry and Biology*; Kohen, A., Limbach, H.-H., Eds.; Springer-Verlag, 2019; pp
1142 796–802.

1143

1144

1145 For Table of Contents use only



1146

1147